RECONSTRUCTION AND UNCERTAINTY QUANTIFICATION OF ENTRY, DESCENT AND LANDING TRAJECTORIES USING VEHICLE AERODYNAMICS

A Thesis
Presented to
The Academic Faculty

by

Prasad M. Kutty

In Partial Fulfillment
of the Requirements for the Degree
Master of Science in the
School of Aerospace Engineering

Georgia Institute of Technology
May 2014

Copyright © 2014 by Prasad M. Kutty

RECONSTRUCTION AND UNCERTAINTY QUANTIFICATION OF ENTRY, DESCENT AND LANDING TRAJECTORIES USING VEHICLE AERODYNAMICS

Approved by:

Professor Alan Wilhite, Advisor
School of Aerospace Engineering
Georgia Institute of Technology

Dr. Christopher Karlgaard
Atmospheric Flight and Entry Systems Branch
Analytical Mechanics Associates, Inc., NASA Langley Research Center

Professor Marcus Holzinger
School of Aerospace Engineering
Georgia Institute of Technology

Date Approved: 2 April, 2014

ACKNOWLEDGEMENTS

I owe a great deal of gratitude to Dr. Chris Karlgaard of Analytical Mechanics Associates for his guidance and advice throughout my thesis research. I am thankful to him for so generously donating his time to my academic pursuits, and providing the support from AMA to perform this work. I would also like to thank my academic advisor, Professor Alan Wilhite, and committee member, Professor Marcus Holzinger for their feedback throughout this process. Their commitment of time and effort has helped shaped this thesis into a work of writing that I am very proud of.

I would like to thank my colleagues at NASA Langley Research Center and AMA. I am grateful to Mark Schoenenberger for sharing his expertise regarding the MSL aerodynamics and for the amazing opportunity to support the MEDLI reconstruction team. I would also like to thank Robert Blanchard for providing valuable insight into previous reconstruction approaches and to Rafael Lugo and Soumyo Dutta for their assistance with various graduate school related issues.

I would like to thank my family and friends whose support has been tremendous. I look forward to spending more of my time with them after the completion of this thesis. Finally, I am especially grateful to my parents. The completion of this thesis is as much a reflection of their hard work as it is mine.

TABLE OF CONTENTS

ACKNOWLEDGEMENTS . . . . . **iii**

LIST OF TABLES . . . . . **vi**

LIST OF FIGURES . . . . . **vii**

NOMENCLATURE . . . . . **ix**

SUMMARY . . . . . **xii**

I INTRODUCTION **1**

1.1 Research Overview 1

1.2 Alternate Reconstruction Methods 4

1.3 Contributions 7

1.4 Outline of Thesis 8

II HISTORICAL PERSPECTIVE **9**

III ADB RECONSTRUCTION ALGORITHM **14**

3.1 Algorithm Equations 16

3.1.1 Air Data Estimation Equations 16

3.1.2 Wind Relative Attitude Estimation Equations 18

3.2 Algorithm Convergence 21

3.3 Applicable Trajectory 24

IV ADB RECONSTRUCTION UNCERTAINTY ANALYSIS **27**

4.1 Fundamentals of Linear Uncertainty Mapping 27

4.2 Uncertainty Analysis Applied to ADB Reconstruction 31

4.2.1 Uncertainty Assessment of Air Data States 32

4.2.2 Uncertainty Assessment of Wind Relative Attitude 34

V APPLICATION OF THE ADB RECONSTRUCTION TO MSL **38**

5.1 MSL EDL Overview 38

5.2 MSL Applicable Trajectory 41

5.3 ADB Reconstruction Inputs for MSL 42

VI RECONSTRUCTION RESULTS 49

6.1 MSL State Reconstructions 49

6.2 MSL State Uncertainties 53

6.3 MSL Uncertainty Sensitivities 57

6.4 Discussion of Results 60

VII CONCLUSIONS AND FORWARD RESEARCH 63

APPENDIX A — EULER INTEGRATION OF HYDROSTATIC EQUATION 65

APPENDIX B — PARTIAL DERIVATIVE EXPRESSIONS FOR AIR DATA UNCERTAINTY ASSESSMENT 66

REFERENCES 68

LIST OF TABLES

1 Chronology and Usage of the ADB Reconstruction Algorithm 13

2 MSL EDL Timeline 40

3 MSL Constant Input Values 43

4 MSL IMU Accelerometer Error Parameters 46

5 MSL Constant Input Uncertainties 47

6 MSL 3-σ Static Aerodynamic Uncertainties 48

LIST OF FIGURES

1 Trajectory Reconstruction Methodologies 3
2 Inertial Reconstruction Flow Diagram 5
3 Extended Kalman Filter Flow Diagram 6
4 Mars Pathfinder Total Angle of Attack Reconstruction Algorithm . . 11
5 Mars Pathfinder Atmosphere Reconstruction Algorithm 12
6 ADB Reconstruction Algorithm Flow Diagram 15
7 Body Frame Definition of the MSL Entry Vehicle 17
8 Surface Plot of C_N/C_A versus Mach and Angle of Attack 22
9 C_N/C_A versus Angle of Attack 22
10 C_N/C_A versus Angle of Attack 23
11 MSL EDL Mission Overview 39
12 MSL RCS Firings During Entry 42
13 MSL Body Acceleration Signals 44
14 MSL Altitude and Velocity 44
15 MSL mass profile 45
16 MSL Body Acceleration Uncertainties 46
17 MSL Altitude and Velocity Uncertainties 47
18 Atmosphere State Estimates 50
19 Air Data State Estimates 51
20 Wind-relative Attitude State Estimates 52
21 Density Uncertainty 53
22 Pressure Uncertainty 54
23 Temperature Uncertainty 54
24 Dynamic Pressure Uncertainty 55
25 Mach Number Uncertainty 55
26 Wind-relative Attitude State Uncertainties 56
27 Density Variance Sensitivities 58

28 Pressure and Temperature Variance Sensitivities 58
29 Air Data State Variance Sensitivities 58
30 Angle of Attack Variance Sensitivities 59
31 Angle of Sideslip Variance Sensitivities 60
32 Number of Iterations Inside of ADB Algorithm 62

NOMENCLATURE

Acronyms

ADB	Aerodynamic Database
CBM	Cruise Balance Mass
CFD	Computational Fluid Dynamics
DDF	Divided Difference Filter
DOF	Desensitized Optimal Filter
EBM	Entry Balance Mass
EDL	Entry, Descent and Landing
EIP	Entry Interface Point
EKF	Extended Kalman Filter
GNC	Guidance, Navigation and Control
IMU	Inertial Measurement Unit
LAURA	Langley Aerothermodynamics Upwind Relaxation Algorithm
MSL	Mars Science Laboratory
MEDLI	Mars Entry, Descent, and Landing Instrumentation
MER	Mars Exploration Rover
MLE	Mars Landing Engine
MPF	Mars Pathfinder
PAET	Planetary Atmosphere Experiments Test
PEPP	Planetary Entry Parachute Program
PF	Particle Filter
RCS	Reaction Control System
SMC	Sequential Monte Carlo
SUFR	Straighten Up and Fly Right
UKF	Unscented Kalman Filter
UPWT	Unitary Plan Wind Tunnel

Symbols

a	Scalar constant used in uncertainty derivation
$\boldsymbol{A}$	Partial derivatives of dynamic model with respect to states

A, B	Random variables
a_x, a_y, a_z	Body axis accelerations at the center of gravity
c	Speed of sound
C_A, C_Y, C_N	Axial, side and normal force coefficients
dp	Pressure of infinitesimally small fluid element
dh	Height of infinitesimally small fluid element
dt	Integration step size
$\boldsymbol{f}$	System of equations used for wind-relative attitude estimation
$\boldsymbol{F}$	Jacobian matrix of the function, f
g	Local acceleration due to gravity
h	Geodetic altitude
$\boldsymbol{J}$	Jacobian Matrix
m	Mass
M	Free-stream mach number
n	Order of derivative
N	Number of observations in a random sample
p	Free-stream static pressure
$\boldsymbol{P}$	Generalized state covariance matrix
$\boldsymbol{Q}$	Process noise matrix
q, r, s, t	Jacobian matrix components for wind-relative attitude
$\bar{q}$	Free-stream dynamic pressure
r_p	Aerocentric planet radius
R	Gas constant of the atmosphere
S	Vehicle reference area
T	Free-stream temperature
$\boldsymbol{u}$	Vector of uncertainty factors for MSL aerodynamic uncertainties
U	Uncertainty factor for MSL aerodynamic uncertainties
u, v, w	Body axis velocities at the center of gravity
V	Free-stream velocity magnitude
$\boldsymbol{w}$	Input vector of function
x	Output of generic function, z
X	Generalized variable used in Euler integration scheme
$\boldsymbol{y}$	Inputs of function $\boldsymbol{f}$, wind-relative attitude
z	Generic function
α	Angle of Attack
β	Angle of Sideslip

γ	Ratio of specific heats
θ	Random variable used in uncertainty derivation
$\lambda_{A,B}$	Cross-covariance of inputs A and B
ρ	Free-stream density
$\rho_{A,B}$	Correlation between inputs A and B
σ	Standard deviation
ϕ	Random variable used in uncertainty derivation

Superscripts

A	Uncertainty adder on MSL aerodynamic uncertainty factor
M	Uncertainty multiplier on MSL aerodynamic uncertainty factor

Subscripts

$Disp$	Dispersed aerodynamic coefficient
j	Current iteration in Newton-Raphson solver
k	Current time step index
Nom	Nominal aerodynamic coefficient

SUMMARY

The reconstruction of entry, descent and landing (EDL) trajectories is significantly affected by the knowledge of the atmospheric conditions during flight. Away from Earth, this knowledge is generally characterized by a high degree of uncertainty, which drives the accuracy of many important atmosphere-relative states. One method of obtaining the in-flight atmospheric properties during EDL is to utilize the known vehicle aerodynamics in deriving the trajectory parameters. This is the approach taken by this research in developing a methodology for accurate estimation of ambient atmospheric conditions and atmosphere-relative states. The method, referred to as the aerodynamic database (ADB) reconstruction, performs reconstruction by leveraging data from flight measurements and pre-flight models. In addition to the estimation algorithm, an uncertainty assessment for the ADB reconstruction method is developed. This uncertainty assessment is a unique application of a fundamental analysis technique that applies linear covariance mapping to transform input variances into output uncertainties.

The ADB reconstruction is applied to a previous mission in order to demonstrate its capability and accuracy. Flight data from the Mars Science Laboratory (MSL) EDL, having successfully completed on August 5th 2012, is used for this purpose. Comparisons of the estimated states are made against alternate reconstruction approaches to understand the advantages and limitations of the ADB reconstruction. This thesis presents a method of reconstruction for EDL systems that can be used as a valuable tool for planetary entry analysis.

CHAPTER I

INTRODUCTION

The exploration of space is an endeavor that has challenged engineers since the first man-made spacecraft was launched into orbit in 1957 [1]. Over the ensuing decades, the scope of space flight has continually broadened as the desired destinations have become progressively more ambitious. Missions to moons, planets and even other solar systems have inspired the continued pursuit of space exploration, while exposing the immense difficulty in doing so. One specific objective in the domain of space flight is the landing of payloads to the surface of planetary bodies. These missions, referred to as entry, descent and landing (EDL), pose unique challenges [2], from the design of an entry system capable of withstanding harsh atmospheric environments to the accurate navigation of the vehicle to a specific location on the planet surface. Despite such obstacles, there have been many successful EDL missions, and the information gathered from each has improved the capability and expanded the objectives of following missions.

In order to learn from a mission with the goal of applying that knowledge to future applications, a post-flight analysis referred to as trajectory reconstruction is employed. Trajectory reconstruction is a form of state estimation by which data taken from onboard instrumentation is used to estimate the vehicle state. The vehicle state is a general term referring to any parameter that provides value in defining the trajectory. Reconstructing the state of the vehicle allows engineers to evaluate vehicle performance, validate pre-flight models and ultimately inform the design of subsequent missions. Many methods of trajectory reconstruction exist in support of these objectives. The research presented in this thesis describes the methodology and application of one such method for EDL reconstruction. The following sections will discuss the objectives for this thesis and the contributions to this field of research.

1.1 Research Overview

When performing trajectory reconstruction for EDL missions, atmosphere-relative states as well as the ambient atmosphere conditions through which the vehicle flew are essential to evaluating vehicle performance. For example, dynamic pressure (a

function of atmospheric density and wind-relative velocity) provides valuable information regarding the heating and structural loading of the vehicle heat shield during entry. Angle of attack and angle of sideslip (functions of wind-relative vehicle velocity) describe the attitude of the vehicle relative to its free-stream velocity, which can be used to gather insight into the in-flight aerodynamics of the vehicle. When designing EDL trajectories, the profiles of atmosphere-relative parameters are usually well known and often engineered to meet the constraints of the system or satisfy the objectives of the mission. After the vehicle has flown, trajectory reconstruction can be applied to recover values of such parameters during flight to understand and explore differences between the actual flight profile and pre-flight predictions. Ultimately, the results of reconstruction analyses can be used to improve knowledge of the vehicle and the atmosphere, allowing future missions to expand their objectives.

Accurate information regarding the entry atmosphere of the planet is necessary for reconstruction of air-relative states. For EDL missions on Earth, precise estimates of the atmosphere structure can be obtained through measurements on the day of flight. These measurements can be obtained from meteorological balloons or rockets instrumented to capture the characteristics of the atmosphere near the geographical vicinity and within an immediate time period of the EDL mission operations. This advantage of accurate atmosphere determination on Earth is not shared by EDL of other planetary bodies. Instead, alternate methods of atmosphere determination must be used.

One commonly used alternate approach to atmosphere structure determination is the use of a reference atmosphere. Applying a reference atmosphere when performing reconstruction carries the limitation of having only a broad measure of the atmosphere. A reference atmosphere does not have the capability to predict small scale atmospheric events (such as wind gusts or off-nominal density deviations) that can arise due to the variability of the atmosphere on a given day at a given location. Therefore, a reference atmosphere must be used with a high level of uncertainty to account for these types of events.

Another approach to atmosphere determination during EDL of other planetary bodies is the use of onboard sensors to provide in-situ measurements of the atmosphere, giving a significantly more precise characterization of the in-flight atmospheric conditions. Examples of this form of instrumentation include air data systems composed of pressure transducers instrumented on the vehicle aeroshell, providing measurements of the entry environment. While these types of data are valuable for accurate air-data estimation, they are not routinely employed by EDL vehicles. To date,

this form of instrumentation on EDL systems has been used sparingly, with mixed success, and solely for the purpose of collecting data. Thus, while in-situ measurements of atmosphere can be used to great advantage for trajectory reconstruction, such instrumentation is not always available. Reconstruction methodologies and results of air data systems used on past entry vehicles are presented in Refs. [3–7].

A third method of gaining insight into the in-flight values of atmosphere through which an entry vehicle flew is applied by this research. Consider the traditional method of reconstruction that couples the knowledge of the vehicle inertial state with the known atmosphere structure to obtain the vehicle aerodynamics and atmosphere-relative trajectory parameters, represented by the flow diagram in Fig. 1(a). An alternate approach to this method is to invert the process by using the known aerodynamics of the vehicle to derive the atmosphere-relative states, shown in Fig. 1(b). Inherent to this approach is the assumption that the vehicle aerodynamics are known more accurately than the atmosphere during entry. For EDL missions, this is generally a valid assumption. This concept of using aerodynamics to derive atmospheric quantities is fundamental to the analysis developed in this thesis.

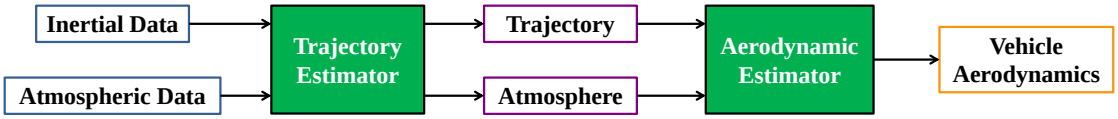

(a) Traditional Reconstruction Approach

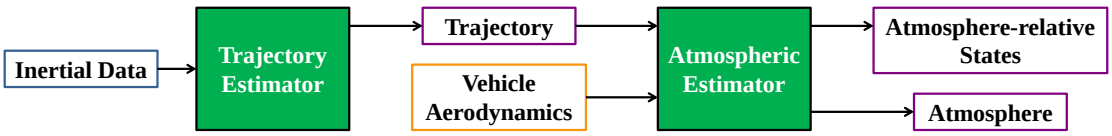

(b) Aerodynamic Reconstruction Approach

Figure 1: Trajectory Reconstruction Methodologies

Additionally, this research utilizes measurements of the applied aerodynamic forces on the vehicle as measured by an onboard inertial measurement unit (IMU). The IMU measurements during entry are compared to the known aerodynamic forces obtained from a pre-flight aerodynamic database to recover estimates of atmosphere-relative parameters as well as the ambient atmospheric conditions during flight. In this manner, state estimates are computed by leveraging data from both flight measurements

and pre-flight models. Unlike the use of a reference atmosphere, this technique does not suffer from the limitation of having very little knowledge of the local atmosphere. In fact, no a priori knowledge of the local atmosphere is required. In addition, the technique does not rely on data from direct, in-situ measurements of the atmosphere, precluding the cost and time required to develop an entry air data system. Instead, only an inertial measurement unit (an accurate and reliable device, commonly used for EDL applications) is required along with the pre-flight vehicle aerodynamics. As such, the reconstruction methodology presented in this thesis is referred to as the aerodynamic database (ADB) reconstruction method.

1.2 Alternate Reconstruction Methods

In order to provide context to the method of reconstruction developed in this research, alternate methods of reconstruction commonly used in post-flight analysis will be described. Specifically, two techniques will be highlighted: a deterministic approach referred to as inertial reconstruction, and a statistical approach known as an extended Kalman filter. When evaluating the results of the ADB reconstruction approach as applied to the Mars Science Laboratory (MSL), the reconstructions using these two methods will be used for comparison.

Inertial reconstruction [8, 9] is a classical approach to trajectory reconstruction by which the state of the vehicle is obtained deterministically through the known dynamics of the vehicle. The dynamics of the vehicle are expressed through equations of motion that describe the rate of change of position, velocity and attitude. Additionally, the applied forces and moments experienced by the vehicle are needed as an input to the equations of motion. The applied forces and moments are recorded during flight in the form of linear accelerations and angular velocity measurements by a system of onboard accelerometers and gyroscopes. Given an initial condition, the equations of motion (expressed as a set of differential equations) are integrated using the acceleration and angular rate measurements as inputs. The integration is performed over the range of measurement data to obtain a reconstructed trajectory. A flow diagram of the inertial reconstruction approach is presented in Fig. 2. The inertial reconstruction conducted for MSL, including the equations of motion, are detailed in Ref. [10].

In addition to estimating the state of the vehicle, the uncertainty of the reconstructed outputs can be obtained using the continuous-time Lyapunov equation [11], given by Eq. 1. This expression defines the dynamics of the state covariance matrix

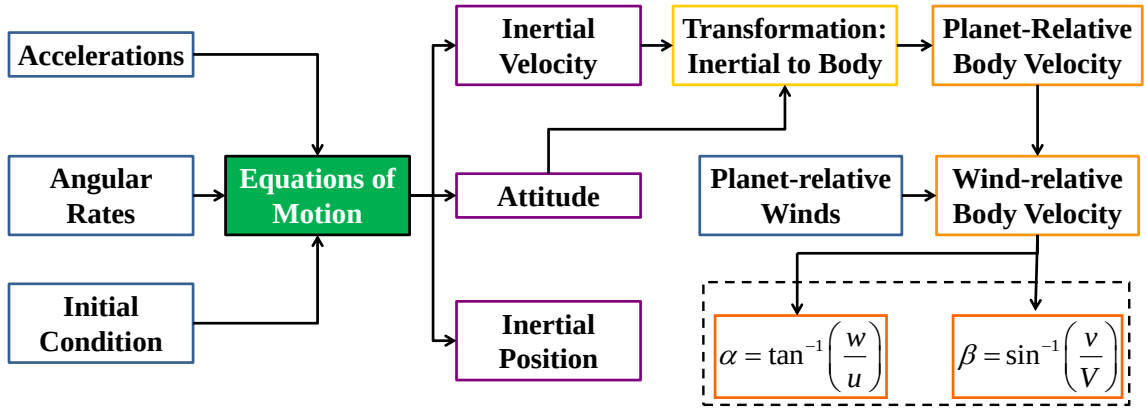

Figure 2: Inertial Reconstruction Flow Diagram

and can be used to propagate the state uncertainties from the initial time to the final time.

$$\dot{\boldsymbol{P}} = \boldsymbol{A}\boldsymbol{P} + \boldsymbol{P}\boldsymbol{A}^T + \boldsymbol{Q} \tag{1}$$

In Eq. 1, $\boldsymbol{P}$ is the state covariance matrix, $\boldsymbol{A}$ is the matrix of partial derivatives of the state dynamics with respect to the state, and $\boldsymbol{Q}$ is the process noise matrix.

It is important to note that the outputs from an inertial reconstruction are inertial or planet-relative, which alone cannot be used for aerodynamic parameter determination. In order to extract the aerodynamic characteristics of the trajectory, some measure of the atmosphere characteristics must be coupled with the inertial reconstruction. For example, an atmosphere-relative (or wind-relative) velocity must be obtained through knowledge of the planet-relative winds in order to obtain a true measure of angle of attack and sideslip. This procedure is shown on the right hand side of Fig. 2. As mentioned in the previous section, the atmosphere structure on Earth can be accurately obtained, but characterization of the atmosphere on other planetary bodies is significantly more challenging. Thus, the use of inertial reconstruction to obtain atmosphere-relative states for EDL missions outside of Earth will carry a level of uncertainty driven by how well the atmosphere is known.

An inertial reconstruction is generally used as the best estimate of the vehicle trajectory when an IMU is the only available source of data from which the vehicle dynamics can be observed. When additional measurements are available, an optimal state estimator can be used to blend these disparate data sources and improve upon the estimates produced by an inertial reconstruction. The extended Kalman filter (EKF) is a widely used optimal state estimator originally developed in the 1960s

for spacecraft navigation [12]. The EKF performs nonlinear state estimation by linearizing the dynamics of the system about the current state estimate. Similar to the inertial reconstruction, equations of motion with inputs of initial condition, accelerations and angular rates are necessary to propagate the state dynamics in order to obtain an initial or a priori state estimate. This a priori estimate is then updated using the observations from the additional measurement sources. For the MSL EDL, additional measurement observations were obtained from a radar altimeter, providing slant range and range rate measurements, a flush air data system, providing measurements of static pressure, a post-flight mesoscale atmosphere model, providing measurements of atmospheric density and pressure, and a landing site location, providing a single observation of the touchdown position. A measurement model expressing each of these observation types as a function of the vehicle state is then used to obtain a predicted measurement given the a priori state estimate. The residual between the predicted and true measurement is used to correct the a priori state estimate and obtain an a posteriori, optimal estimate of the vehicle state. A flow diagram of the EKF algorithm is presented in Fig. 3, and a more detailed description of the EKF can be found in Ref. [11]. The application of the EKF to the MSL mission is described in Ref. [13].

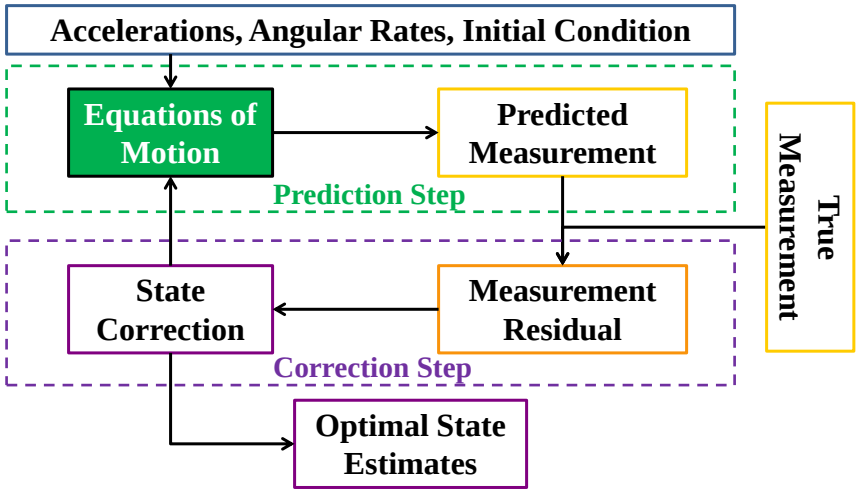

Figure 3: Extended Kalman Filter Flow Diagram

An inherent advantage to the use of an EKF for trajectory reconstruction is that uncertainties are computed internally by the estimator. The state covariance, along with the measurement residual, is used to correct the a priori state estimate and therefore must also be propagated (using Eq. 1) and updated. In this manner, the

EKF very conveniently generates optimal state estimates and their associated uncertainties. While the inertial reconstruction technique can be classified as deterministic, the EKF algorithm falls under the class of statistical estimators. Other examples of statistical estimators include the unscented Kalman filter [11] (UKF), particle filter [11] (PF) or sequential Monte Carlo (SMC), divided difference filter [14] (DDF) and desensitized optimal filter [15] (DOF). Any of these methods can be applied for the purposes of trajectory reconstruction.

1.3 Contributions

The purpose of this thesis is to develop a method of EDL trajectory reconstruction that can be applied when the atmospheric properties are poorly known. The analysis developed in this research is founded in past analyses but carries several features that have not been previously implemented. The ADB reconstruction method presented here improves upon previous algorithms by coupling the estimation of air data states and wind-relative attitude. A two loop algorithm architecture, one to compute air data states and one to compute wind-relative attitude, is utilized to converge upon a best estimate of the reconstructed state. Additionally, the algorithm constructs a system of non-linear equations expressing a relationship between the ratios of aerodynamic force coefficients that can be solved to generate estimates of angle of attack and angle of sideslip. Previous versions of this reconstruction approach have produced estimates of only angle of attack or total angle of attack.

In addition to the reconstruction algorithm, an uncertainty analysis is developed to provide insight into the accuracy of the reconstructed states. The uncertainty assessment, which relies on linear covariance transformations to compute the variances of state estimates, has not previously been applied to the ADB reconstruction algorithm. These three aspects of the analysis, (1) a two loop algorithm to refine parameters estimates and converge upon a final solution, (2) obtaining both angle of attack and sideslip from the estimator and (3) performing an uncertainty assessment through linear covariance mapping, are new to this field of reconstruction.

The ADB reconstruction will also be applied to a previous mission in order to demonstrate its capability and accuracy. Flight data from the MSL EDL, having successfully completed on August 5th 2012, will be used for this purpose. State reconstructions and uncertainty estimates using the ADB reconstruction will be presented and comparisons will be made to solutions from other reconstruction techniques. The following thesis research will provide current and future engineers with an analysis

tool that is well documented, well tested and a useful resource for analysts seeking to perform accurate reconstruction of attitude and atmosphere during planetary entry missions.

1.4 Outline of Thesis

The remaining sections in this thesis are divided as follows:

- Chapter 2 describes the historical development of the ADB reconstruction methodology. The evolution of the algorithm from its initial implementation to its current application is discussed. Many of these past analyses were utilized for previous EDL missions, and their chronology is outlined with regards to the reconstruction approach.

- Chapter 3 provides an overview of the ADB algorithm and the specific equations used to perform reconstruction. The estimation equations for air data states and wind-relative attitude are detailed. The range of valid regions during an EDL trajectory for performing ADB reconstruction are also explained.

- Chapter 4 details the method of uncertainty assessment used for the reconstructed states. The technique, known as linear covariance mapping, is derived and applied to the ADB reconstruction. The derivation is extended to the estimation equations for density and wind-relative attitude, with the remaining partial derivative expressions provided in Appendix B.

- Chapter 5 discusses the MSL EDL mission, and the application of the ADB reconstruction to the MSL flight data. The portion of the trajectory best suited for ADB reconstruction is highlighted, and the inputs used to perform the reconstruction over that region are described.

- Chapter 6 presents the results of the ADB reconstruction applied to the MSL entry. The state estimates and uncertainties are compared to alternate methods of reconstruction. The uncertainty sensitivities are outlined in order to provide insight into the driving uncertainties of each state. The results are discussed and some notes are made regarding convergence of the algorithm.

- Chapter 7 provides some concluding remarks regarding this thesis research and potential forward work in this area of study.

CHAPTER II

HISTORICAL PERSPECTIVE

The method of reconstruction used in the following research has been applied to a variety of missions, both research and operational, over the past half century. A literature search of EDL missions since the 1960s has demonstrated the usefulness of the ADB reconstruction method for planetary entry missions. The ADB reconstruction approach utilizes in situ measurements of acceleration to characterize ambient atmosphere conditions and atmosphere-relative states. Because the technique does not rely on an accurate atmosphere model for reconstruction, it is particularly well suited for entry reconstruction on planets other than Earth, where limited atmosphere information is available. As such, this method has been utilized or proposed only for entry of other planetary bodies. The following section provides an overview of the history and development of the ADB reconstruction method.

The reconstruction of atmosphere states (density, pressure, and temperature) using the technique relied upon by the ADB reconstruction has been previously explored in varying forms. The earliest found reference to such an analysis was presented in 1963 by Seiff [16], in which the method used by the ADB reconstruction to compute density and pressure was first proposed. Density is estimated through rearrangement of the drag force equation while pressure is computed through the hydrostatic equation. These equations are outlined in Chapter 3.1.1. This method of atmosphere structure determination is a simple, non-iterative method proposed for probe vehicles entering the atmospheres of Mars and Venus but was first applied to Earth-based flight tests, such as the Planetary Entry Parachute Program [17] (PEPP) and the Planetary Atmosphere Experiments Test [18] (PAET). In some instances, it has been modified to improve the estimation accuracy. For example, a parametric approach was taken by Sommer [17] to determine values of density and pressure, which were then used to compute Mach number. The updated value of Mach number was then used in the parametric analysis to re-estimate density and pressure, and this cycle was repeated until all of the estimated states had converged. The method originally proposed by Seiff is still considered the classical approach for EDL atmosphere reconstruction and has since been utilized by various missions, including Pioneer Venus [19], Galileo [20], Mars 6 [21], Venera 7 [22], Huygens [23], Mars Pathfinder [24], Mars Exploration

Rover [25] (MER), and Mars Phoenix Lander [26].

The use of force and acceleration ratios to compute wind-relative attitude was first presented in 1965 by Seiff and Reese [27], in which a trigonometric relationship is proposed between accelerations measured by accelerometers and aerodynamic forces obtained through wind tunnel measurements (as computational methods were not available to engineers in 1965). The relationship is an implicit function of angle of attack and was solved numerically, although little detail is provided on the algorithm used to do so. While the relationship given by Seiff and Reese is not exactly the same as that used by the ADB reconstruction, it forms the root of the current method.

In preparation for the Viking missions that landed on Mars in 1976, Nier et al. described the method [28] of angle of attack and atmosphere reconstruction that closely resembles the ADB reconstruction used in this research. Density and pressure are estimated through the drag force equation and the hydrostatic equation, respectively. A ratio of normal to axial acceleration, which is functionally dependent on angle of attack, is used to estimate wind-relative attitude. The proposed function is characterized from wind tunnel test data, and an assumption is made that the ratio is linearly related to the angle of attack. Because of the linear assumption, angle of attack can be directly computed without the need for an iterative algorithm. While this assumption is not used or needed for the present ADB reconstruction method, the method proposed by Nier et al. is conceptually related.

The ADB reconstruction method of estimating wind-relative attitude was further explored and utilized for the Mars Pathfinder trajectory reconstruction [24]. Similar to what was done by Nier et al. [28], the aerodynamic database is used to recover the total angle of attack [24]. This was done by identifying the total angle of attack that satisfied the relationship, $(a_N/a_A) = (C_N/C_A)$. The normal and axial accelerations are obtained from the IMU at each time step. Mach number at each time step is obtained from velocity, through inertial reconstruction, and temperature from a reference atmosphere. In order to evaluate the equality, $(a_N/a_A) = (C_N/C_A)$, the aerodynamic database is queried at the current Mach number over a range of total angle of attack values to obtain normal and axial force coefficient profiles, and subsequently the ratio of force coefficients, C_N/C_A, over that total angle of attack range. This range of values is chosen through a priori knowledge of the flight trajectory (likely a pre-flight nominal reference trajectory), such that the true total angle of attack will fall inside of that range. Then, the C_N/C_A profile over the selected total angle of attack range is interpolated to the acceleration ratio at the current time step in order to compute the total angle of attack at the current time. The

Mars Pathfinder technique for total angle of attack reconstruction differs from the ADB reconstruction algorithm presented in this thesis as it is not updated through iteration. After total angle of attack is computed through interpolation, the process described above is repeated at the next time step. Additionally, angle of sideslip is not obtained by the reconstruction. A flow diagram presenting the total angle of attack reconstruction technique used by Mars Pathfinder is shown in Fig. 4.

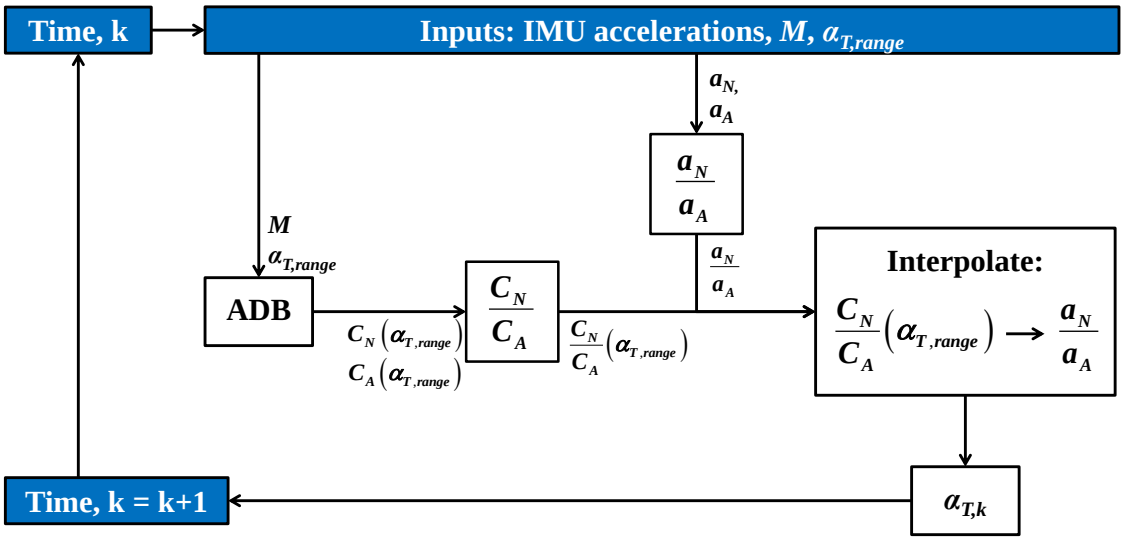

Figure 4: Mars Pathfinder Total Angle of Attack Reconstruction Algorithm

In addition to the total angle of attack reconstruction, an atmosphere profile for Mars Pathfinder was derived using an iterative algorithm to reconstruct density, pressure, temperature and Mach number [29]. The algorithm begins with an a priori estimate of axial force coefficient, which, beginning at hypersonic entry, is a relatively constant value. This initial estimate of axial force coefficient is then used to compute density, followed by pressure, temperature and Mach number. The computations for these air data states are similar to those used in the ADB reconstruction algorithm, and will be presented in Section 3.1.1. The computed Mach number is passed to the aerodynamic database along with total angle of attack (calculated by the method shown in Fig. 4) to obtain an updated value of axial force coefficient. This updated value is compared to the original estimate, and if their difference is larger than a chosen threshold, the process is repeated by using the new value of axial force coefficient to compute the air data states. Usually this method takes only a small number of iterations to converge upon final values of density, pressure, temperature and Mach number [29]. A flow diagram presenting the Mars Pathfinder method of atmosphere structure reconstruction is given in Fig. 5. Unlike the Mars Pathfinder algorithm, the

ADB reconstruction method developed for this research performs estimation of air data states and wind-relative attitude concurrently, which is an important distinction between previous reconstruction techniques and the analysis to be conducted here.

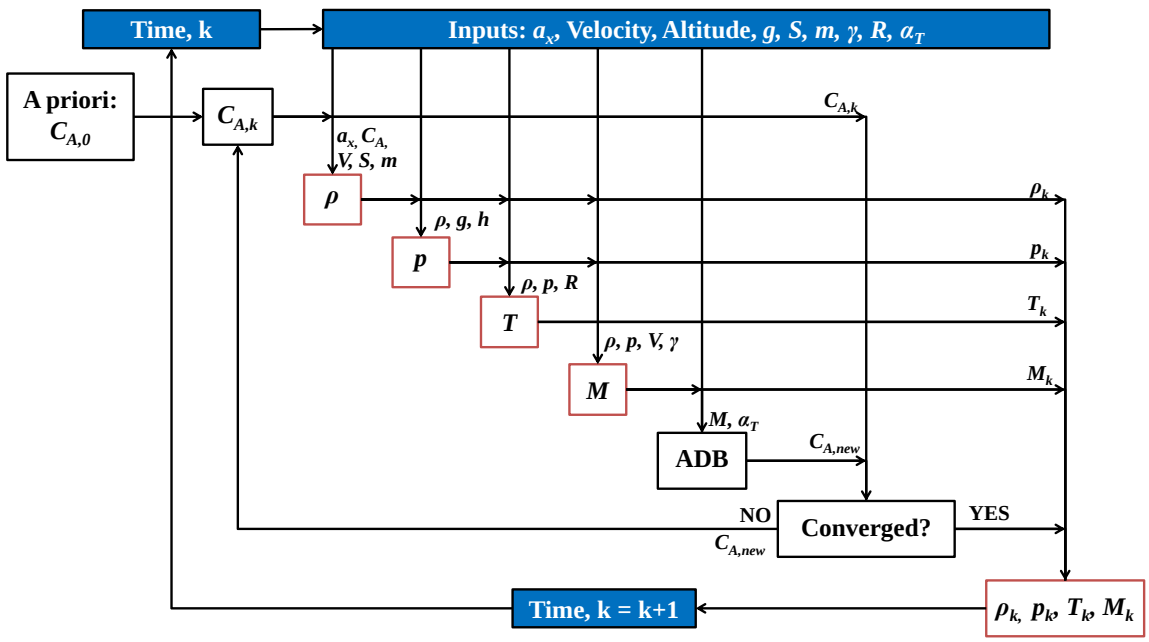

Figure 5: Mars Pathfinder Atmosphere Reconstruction Algorithm

An overview of previous applications of the ADB reconstruction method in chronological order are presented in Table 1. The list identifies the analysis by the author and project, and the source for each analysis is given in the references section. For each analysis, additional information is provided indicating computed atmosphere states and wind-relative attitude using the vehicle aerodynamics. The analyses in Table 1 lay the framework for the ADB reconstruction method presented and detailed in this thesis research.

Table 1: Chronology and Usage of the ADB Reconstruction Algorithm

Year	Author [Reference]	Program	Atmosphere Reconstruction	Attitude Reconstruction
1963	Seiff [16]	None	Yes	No
1965	Peterson [30]	None	Yes	No
1965	Seiff, Reese [27]	None	Yes	Yes
1968	Seiff [31]	None	Yes	No
1968	Sommer, Yee [17]	PEPP[a]	Yes	Yes
1969	Seiff [32]	None	Yes	No
1971	Avduevsky, et al. [22]	Venera 7	Yes	No
1972	Nier, et al. [28]	Viking	Yes	Yes
1973	Seiff et al. [18]	PAET[b]	Yes	No
1977	Kerzhanovich [21]	Mars 6	Yes	No
1980	Seiff et al. [19]	Pioneer	Yes	No
1997	Seiff [20]	Galileo	Yes	No
1999	Magalhaes, et al. [33]	MPF[c]	Yes	No
1999	Spencer, et al. [24]	MPF	Yes	Yes
2003	Withers, et al. [34]	MPF	Yes	Yes
2005	Atkinson, et al. [35]	Huygens	No	Yes
2006	Withers, Smith [25]	MER[d]	Yes	No
2007	Kazeminejad, et al. [23]	Huygens	Yes	No
2008	Colombatti, et al. [36]	Huygens	Yes	Yes
2010	Withers [37]	None	Yes	No
2011	Blanchard, Desai [26]	Phoenix	Yes	No

[a]Planetary Entry Parachute Program
[b]Planetary Atmosphere Experiments Test
[c]Mars Pathfinder
[d]Mars Exploration Rover

CHAPTER III

ADB RECONSTRUCTION ALGORITHM

The ADB reconstruction algorithm is a method of trajectory reconstruction used to recover estimates of: (1) the free-stream air data characteristics of the atmosphere through which the vehicle flew, and (2) the wind-relative attitude of the vehicle. A high level depiction of the ADB reconstruction algorithm is presented in Fig. 6. The algorithm is an iterative technique consisting of two loops. An outer loop computes air data estimates of density, pressure, Mach number, temperature and dynamic pressure. An inner loop performs reconstruction of wind relative attitude, specifically angle of attack and angle of sideslip. These two loops are evaluated in sequence until the parameters computed inside of both loops converge. The blue lines delineate the outer loop used to compute the air data states. The inner loop of the algorithm resides in the green box where ratios of accelerations and force coefficients are used to determine wind-relative attitude.

The algorithm begins with the outer loop by querying the aerodynamic database to obtain axial force coefficient. The outer loop is initialized using a priori estimates of angle of attack, angle of sideslip and Mach number as inputs to the aerodynamic database. Axial force coefficient is then used to compute density, and density is used to compute the remaining air data states. The specific equations used to compute the air data states are detailed in Section 3.1.1. At this point, the calculations in the outer loop are complete and the algorithm proceeds to the inner loop.

The inner loop applies a Newton-Raphson solver to compute the roots of a system of non-linear equations in order to reconstruct angle of attack and angle of sideslip. The equations, detailed in Section 3.1.2, express a relationship between the vehicle acceleration (as measured by the IMU) and the force coefficients from the aerodynamic database, to which Mach number (computed in the outer loop) is an input. Obtaining the roots to the system of equations yields the angle of attack and sideslip at the current flight condition. Once the Newton-Raphson algorithm has converged, the updated wind-relative attitude is returned to the outer loop to query the aerodynamic database and recompute the air data states. The handoff between these two loops continues until the estimated parameters converge on a final solution.

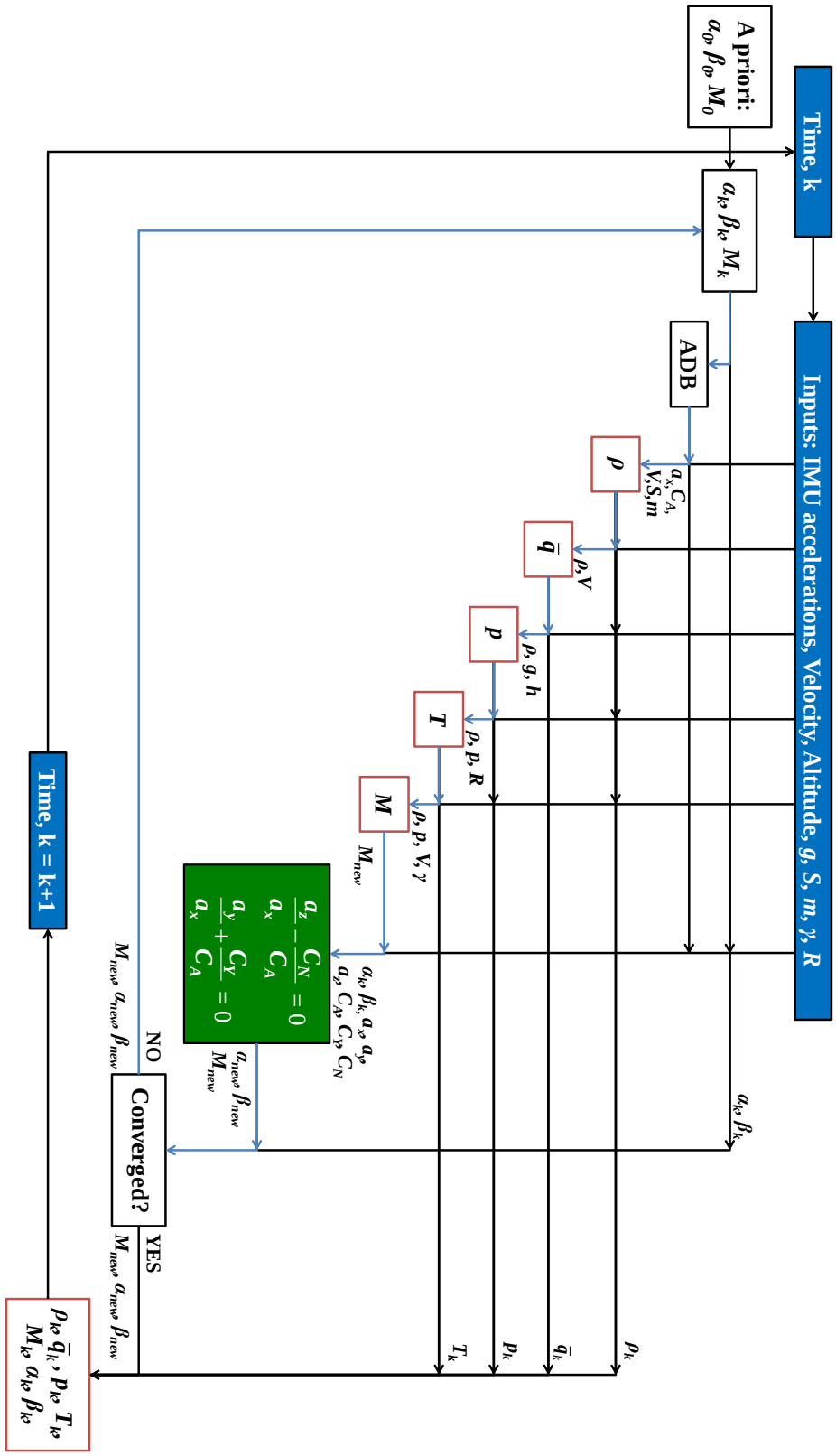

Figure 6: ADB Reconstruction Algorithm Flow Diagram

3.1 Algorithm Equations

The following sections detail the estimation equations used by the ADB algorithm to perform reconstruction of the output states. Section 3.1.1 describes the expressions used for estimation of the air data states: density, pressure, Mach number and temperature. Section 3.1.2 describes the expressions used for estimation of the angle of attack and sideslip.

3.1.1 Air Data Estimation Equations

Reconstruction of the air data estimates is performed in the outer loop of the algorithm. For each time point in the reconstruction, the first step in the outer loop is to query the aerodynamic database to obtain axial force coefficient. In general, the aerodynamic database is a function of angle of attack, angle of sideslip and Mach number. Because these states are estimated inside of the reconstruction algorithm, an a priori estimate of their values are obtained to initialize the estimator. For angle of attack and sideslip, an inertial or deterministic reconstruction can be performed to obtain a priori, planet-relative estimates of these states. Mach number can be computed using the reconstructed inertial velocity and a reference atmosphere. At the first time point in the reconstruction, these a priori estimates can be used to initiate the algorithm. At every subsequent time point, the estimates of these states at the previous time can be used.

For reference, the MSL body frame is shown in Fig. 7 and the corresponding definitions of axial, side and normal force coefficient are given. Once the axial force coefficient is retrieved from the aerodynamic database, the definition of axial force coefficient is inverted to obtain density, as shown by Eq. 2 and Eq. 3:

$$C_A = -\frac{2ma_{x,k}}{\rho_k {V_k}^2 S} \tag{2}$$

$$\rho_k = -\frac{2ma_{x,k}}{{V_k}^2 S C_A} \tag{3}$$

In Eq. 3, m is the vehicle mass, $a_{x,k}$ is the x-axis (or axial) acceleration, V_k is the vehicle velocity, S is the reference area of the vehicle and C_A is the axial force coefficient extracted from the aerodynamic database. Recall that velocity was obtained during the inertial reconstruction of the trajectory. Note that throughout this section, the subscript k will be used to denote estimates at the current time.

Next, the hydrostatic equation is used to compute free-stream static pressure. The

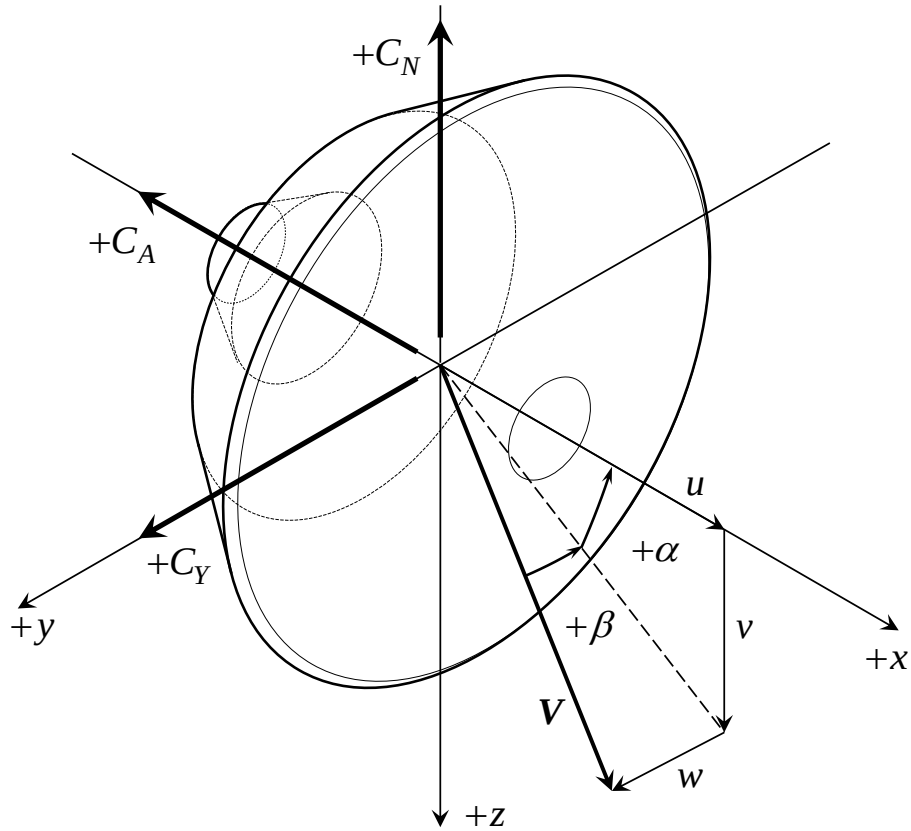

Figure 7: Body Frame Definition of the MSL Entry Vehicle

hydrostatic equation is given by the following relationship:

$$dp = -\rho g dh \tag{4}$$

In this expression, dp and dh are the pressure and height of an infinitesimally small fluid element with density, ρ, and local acceleration due to gravity, g. In order to estimate pressure inside of the ADB algorithm, a first order Euler integrator is applied to the hydrostatic equation. The resulting equation, derived in Appendix A, is given by:

$$p_k = p_{k-1} - \rho_k g_k \left(h_k - h_{k-1}\right) \tag{5}$$

In Eq. 5, the current pressure, p_k, is a function of the differential in altitude between the current and previous times, $h_k - h_{k-1}$, as well as the current density, ρ_k, and local acceleration due to gravity, g_k. The local gravity is computed through the following equation [38] where, where μ is the gravitational parameter of the planet and $r_{p,k}$ is the distance from the planet center to the vehicle:

$$g_k = \frac{\mu}{r_{p,k}^2} \tag{6}$$

Having computed the pressure, Mach number is calculated from the speed of sound through the following definitions:

$$c_k = \sqrt{\gamma \frac{p_k}{\rho_k}} \tag{7}$$

$$M_k = \frac{V_k}{c_k} \tag{8}$$

In these equations, c_k is the speed of sound, γ is the ratio of specific heats of the atmosphere and M_k is the Mach number. Next, temperature is computed using the equation of state:

$$T_k = \frac{p_k}{R\rho_k} \tag{9}$$

In Eq. 9, R is the gas constant for the atmosphere. The final air data estimate computed in the outer loop is dynamic pressure, $\bar{q}_k$, as given by the following definition:

$$\bar{q}_k = \frac{1}{2}\rho_k {V_k}^2 \tag{10}$$

After these states are computed, the inner loop of the algorithm is initiated to estimate angle of attack and sideslip.

3.1.2 Wind Relative Attitude Estimation Equations

The inner loop of the ADB algorithm performs reconstruction of the wind relative attitude of the vehicle by applying a Newton-Raphson root solver to a system of non-linear equations. This system of equations is derived through a ratio of force coefficients. The force coefficients in each axis are defined by Eqs. 11-13 as:

$$C_A = -\frac{ma_x}{\bar{q}S} \tag{11}$$

$$C_N = -\frac{ma_z}{\bar{q}S} \tag{12}$$

$$C_Y = \frac{ma_y}{\bar{q}S} \tag{13}$$

In these equations, the x, y and z-axes are vehicle body axes, and the force coefficient direction is defined according to the convention used for the MSL aerodynamics, shown in Fig. 7. In general, the signs on the right hand side of Eqs. 11-13 should maintain a consistent direction between force coefficient and acceleration. For example, if the z-axis of the body frame points upward, parallel to the direction of normal force, then the negative sign on the right hand side of Eq. 12 should not be used.

Using these definitions of force coefficients, the ratios of normal and side force to axial force are evaluated. First, the ratio of normal force to axial force is given by:

$$\frac{C_N}{C_A} = \frac{-\frac{ma_z}{\bar{q}S}}{-\frac{ma_x}{\bar{q}S}} \tag{14}$$

$$\frac{C_N}{C_A} = \frac{a_z}{a_x} \tag{15}$$

For a given Mach number, the left hand side of Eq. 15 is a function of angle of attack and sideslip. A more formal representation of Eq. 15 can be expressed by:

$$\frac{C_N}{C_A}(\alpha, \beta) = \frac{a_z}{a_x} \tag{16}$$

Now this equation is rearranged so that one side of the equation is equal to zero:

$$\frac{C_N}{C_A}(\alpha, \beta) - \frac{a_z}{a_x} = 0 \tag{17}$$

Next, a similar ratio is evaluated for side force and axial force:

$$\frac{C_Y}{C_A} = \frac{\frac{ma_y}{\bar{q}S}}{-\frac{ma_x}{\bar{q}S}} \tag{18}$$

$$\frac{C_Y}{C_A} = -\frac{a_y}{a_x} \tag{19}$$

As with the ratio of normal to axial force coefficient, the ratio expressed in Eq. 19 is also a function of angle of attack and sideslip for a given Mach number. A more formal expression for Eq. 19 is shown by:

$$\frac{C_Y}{C_A}(\alpha, \beta) = -\frac{a_y}{a_x} \tag{20}$$

Eq. 20 can also be rearranged to equal zero:

$$\frac{C_Y}{C_A}(\alpha, \beta) + \frac{a_y}{a_x} = 0 \tag{21}$$

Eq. 17 and Eq. 21 provide the nonlinear system of equations needed to solve for angle of attack and sideslip. Both equations are functions of angle of attack and sideslip and both equations have been set equal to zero. As such, a root finding algorithm can be applied to solve the system of equations at the current flight condition, yielding the wind relative attitude of the vehicle. More succinctly, this pair of functions can be written as:

$$\boldsymbol{f}(\boldsymbol{y_k}) = \boldsymbol{f}(\alpha_k, \beta_k) = \begin{Bmatrix} f_1(\alpha_k, \beta_k) \\ f_2(\alpha_k, \beta_k) \end{Bmatrix} = \begin{Bmatrix} \frac{C_N}{C_A}(\alpha_k, \beta_k) - \frac{a_{z,k}}{a_{x,k}} \\ \frac{C_Y}{C_A}(\alpha_k, \beta_k) + \frac{a_{y,k}}{a_{x,k}} \end{Bmatrix} = \begin{bmatrix} 0 \\ 0 \end{bmatrix} \tag{22}$$

In Eq. 22, $\boldsymbol{y_k}$ is the set of independent variables, angle of attack and sideslip at the current time, to the system of equations. At each time point, this function is evaluated and solved using a Newton-Raphson solver. The force coefficients are obtained from the aerodynamic database. As with the initialization of the outer loop, an a priori estimate of angle of attack and sideslip obtained from inertial reconstruction is used to call the database. Instead of a priori data, the Mach number computed in the outer loop (Eq. 8) is used to query the aerodynamic database. These initial states are used to begin the Newton-Raphson algorithm in seeking the roots to the system of equations.

The Newton-Raphson method is a simple, but powerful root solving technique that uses the derivative of the function to iteratively converge upon the root of an equation [39]. Each iteration of the solver updates the estimate of the root from the previous iteration. An initial guess is needed, and the time required to find the solution to the equation is dependent on the quality of the initial guess. The update equation for the Newton-Raphson solver is:

$$\boldsymbol{y}_{k,j} = \boldsymbol{y}_{k,j-1} - \boldsymbol{F}(\boldsymbol{y}_{k,j-1})^{-1} \boldsymbol{f}\left(\boldsymbol{y}_{k,j-1}\right) \tag{23}$$

In Eq. 23, the j subscript refers to the current iteration in the root solving algorithm and $\boldsymbol{F}\left(\boldsymbol{y}_{k,j-1}\right)$ is the matrix of partial derivatives of the function, $\boldsymbol{f}$, with respect to the dependent variables evaluated at the previous iteration. For use with the system of equations expressed by Eq. 22, the roots of the function $\boldsymbol{f}\left(\boldsymbol{y}_k\right)$ are the value of angle of attack and sideslip at the current flight condition. This update equation as applied to Eq. 22 is given by:

$$\begin{bmatrix} \alpha_{k,j} \\ \beta_{k,j} \end{bmatrix} = \begin{bmatrix} \alpha_{k,j-1} \\ \beta_{k,j-1} \end{bmatrix} - \begin{bmatrix} \frac{\partial f_1}{\partial \alpha_{k,j-1}} & \frac{\partial f_1}{\partial \beta_{k,j-1}} \\ \frac{\partial f_2}{\partial \alpha_{k,j-1}} & \frac{\partial f_2}{\partial \beta_{k,j-1}} \end{bmatrix}^{-1} \begin{bmatrix} \frac{C_{N,k,j-1}}{C_{A,k,j-1}} - \frac{a_{z,k}}{a_{x,k}} \\ \frac{C_{Y,k,j-1}}{C_{A,k,j-1}} + \frac{a_{y,k}}{a_{x,k}} \end{bmatrix} \tag{24}$$

Once the Newton-Raphson algorithm converges, the updated values of angle of attack and sideslip have been obtained and are passed back to the outer loop. The outer loop is restarted by querying the aerodynamic database to look up axial force coefficient and compute the air data states expressed by Eqs. 3-10. This exchange between inner and outer loop of the ADB reconstruction algorithm is continued until the wind relative attitude estimates, and consequently, the air data states converge.

3.2 Algorithm Convergence

In applying the ADB algorithm, some care must be taken to provide the estimator with a reasonably accurate initial estimate of angle of attack, sideslip and Mach number. If these initial values are significantly different from the solution, the algorithm may either converge upon physically unreasonable estimates of angle of attack and sideslip or update their values incorrectly. The first issue related to convergence is the potential to obtain flawed estimates of wind-relative attitude if significant error exists in Mach number. Recall that the inner loop estimator computes angle of attack and sideslip using the aerodynamic database at a given Mach number. For any inaccuracy in Mach number, the incorrect region of the aerodynamic database will be used to recover wind-relative attitude.

This issue can be examined visually through a surface plot of the force coefficient ratio, C_N/C_A, versus Mach number and angle of attack. As an example, the MSL aerodynamic database is used to obtain values of C_N/C_A over a range of angles of attack (-30 to 30 degrees) and a range of Mach numbers (16 to 24) as shown by Fig. 8. The ADB algorithm performs reconstruction by extracting the profile of C_N/C_A versus angle of attack at the current Mach number, selected to be Mach 20 for the purposes of this example. This profile represents the intersection of the green plane and the blue surface. The resulting curve is shown in Fig. 9 (note that the left sub-figure is the entire curve, and the right sub-figure is zoomed in to distinguish the intersections). Next, angle of attack is obtained by finding the intersection of this curve with the current ratio of accelerations, a_z/a_x. At this flight condition, a_z/a_x observed by the IMU is -0.0387 and is shown by the dashed, magenta line in Fig. 9. The intersection of the two curves yields a reconstructed angle of attack for the Mach 20 case of -16.7731 degrees.

Now consider the solution if Mach 17 is used as the given Mach number instead of Mach 20. The intersecting plane for this condition is shown in red in Fig. 8. The resulting C_N/C_A curve, also shown in Fig. 9, lies very nearly on top of the curve at Mach 20. For this Mach 17 profile, the reconstruction algorithm would yield an angle of attack of -17.0839 degrees - a difference of 0.3108 degrees from the angle of attack reconstructed from the Mach 20 profile. This result shows a relative insensitivity of the reconstructed angle of attack to variations in Mach number, as expected during hypersonic flight. An error of Mach 3 equates to less than a third of a degree of error in angle of attack for this example. Thus, although an accurate initial estimate of Mach number should be used inside of the estimator, the wind-relative attitude

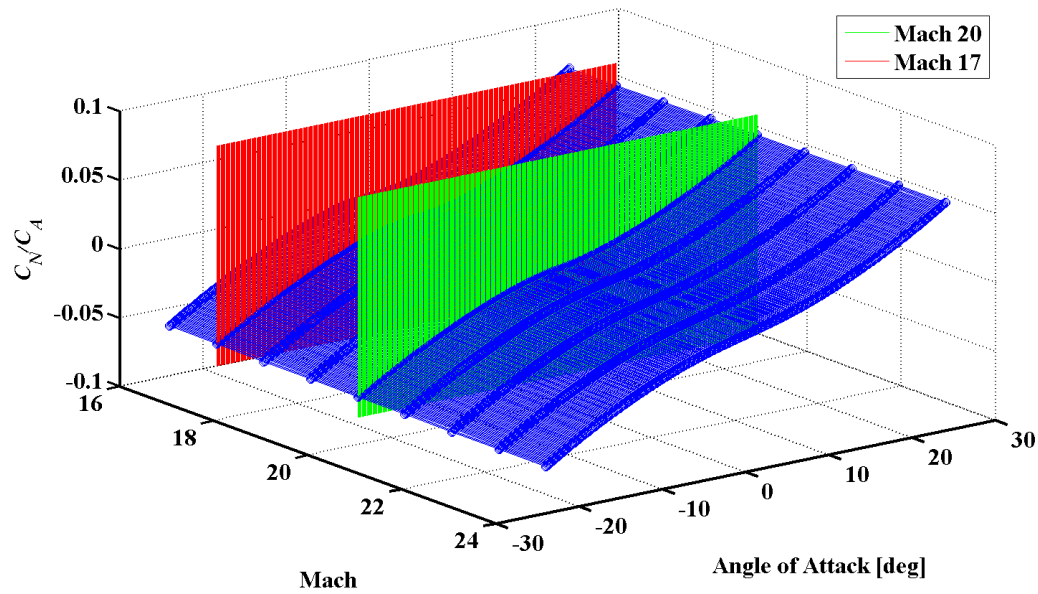

Figure 8: Surface Plot of C_N/C_A versus Mach and Angle of Attack

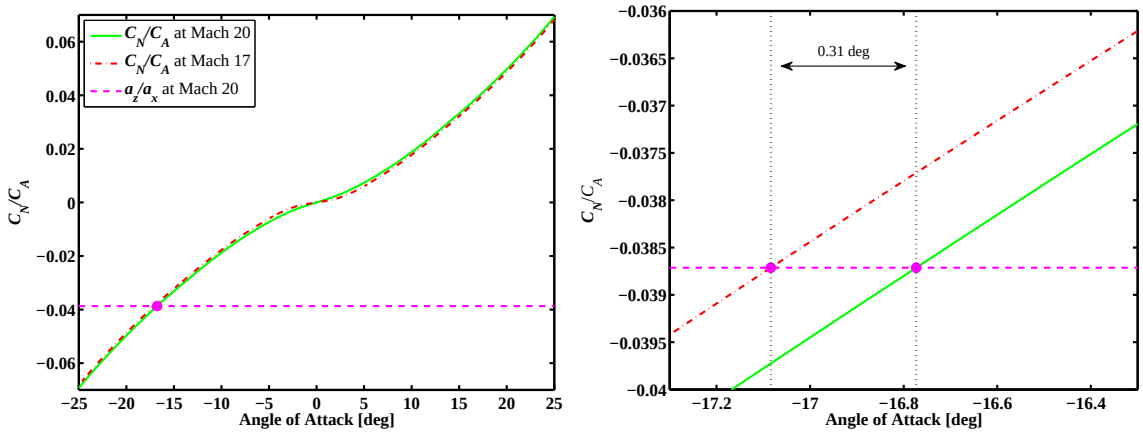

(a) C_N/C_A extracted from Figure 8

(b) C_N/C_A zoomed in

Figure 9: C_N/C_A versus Angle of Attack

reconstruction does display a reasonable level of robustness against significant Mach errors.

The second issue related to algorithm convergence can arise if the Newton-Raphson algorithm finds a value of wind-relative attitude that satisfies the coefficient ratios, Eq. 22, in the incorrect region of the aerodynamic database. To explore this issue, the force coefficient ratio, C_N/C_A, is examined over a large range of angle of attack values to assess the potential for multiple solutions. Note that for this exercise an Apollo aerodynamic database [40] is used because the MSL aerodynamic database is only

valid for values of total angle of attack less than 24 degrees. The Apollo aerodynamics are extracted at an arbitrary Mach number, chosen to be Mach 20 for the purposes of this example. The values of C_N/C_A are shown in Fig. 10 with the range of angle of attack extended in order to observe other potential intersections with the a_z/a_x value. In this example, a_z/a_x was selected to equal 0.1.

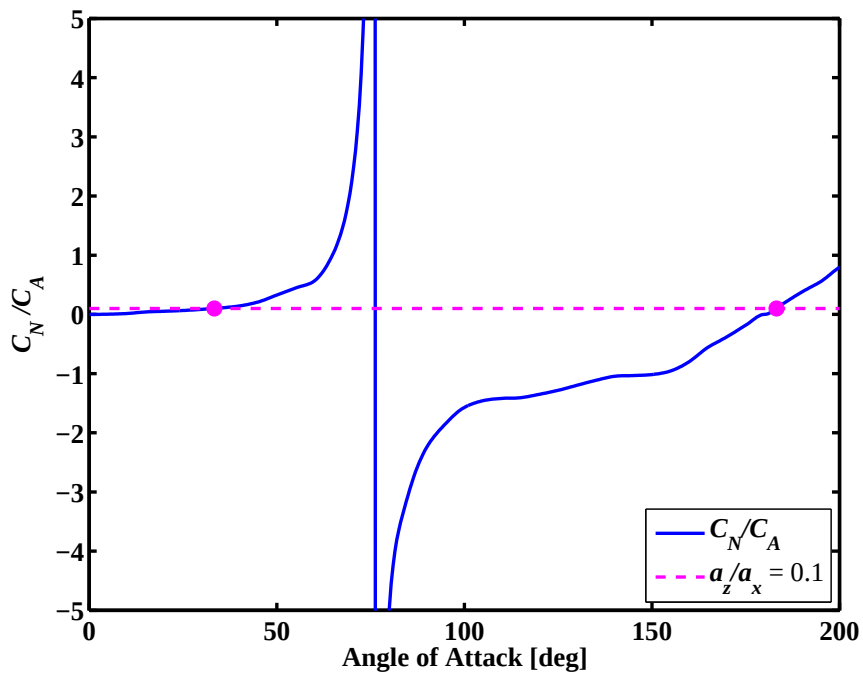

Figure 10: C_N/C_A versus Angle of Attack

The ratio of force coefficients resembles a tangent function with an asymptote at approximately 76 degrees, representing the transfer of aerodynamic force from the axial direction to the normal direction as angle of attack departs from zero degrees. Because the tangent function repeats every 180 degrees, the potential exists for the Newton-Raphson algorithm to find a value of C_N/C_A that equals the acceleration ratio at a different angle of attack. As seen in Fig. 10, the first value of angle of attack to satisfy the selected condition, $a_z/a_x = 0.1$, is 33.36 degrees. The next value of angle of attack to satisfy this condition is 183.2 degrees, a difference of nearly 150 degrees. Thus, a very poor initial estimate of angle of attack would be needed to converge upon an incorrect solution, and this type of error would be easily recognized due to its inconsistence with the expected dynamics of the vehicle. During post-processing, an analyst could recognize an erroneous result, improve the initial estimate and repeat the root search in order to recover the correct angle of attack. While a Newton solver

does not guarantee convergence towards the desired root, the aerodynamic characteristics of most blunt body entry vehicles provide some robustness against this type of error. Additionally, generating initial estimates through inertial reconstruction will provide initial values of the accuracy necessary to avoid this convergence issue.

3.3 Applicable Trajectory

As described in Section 3.1.2, the ADB reconstruction algorithm relies on the comparison between the aerodynamic database of the vehicle and the IMU measurements recorded during flight. An inherent limitation of this method is the requirement of consistency between these two data sets in order for their comparison to be valid. All of the forces acting on the vehicle, as measured by the IMU, must be represented by the aerodynamic force coefficients used in the algorithm. Therefore, it is important to understand the significance of the measurements (specifically of acceleration) recorded by the IMU.

The use of an IMU to measure the motion of a moving vehicle can be traced back several decades for the purpose of inertial navigation [8]. In fact, inertial navigation in this form is a modern practice of dead reckoning, by which the position of a vehicle in inertial space can be determined through measurements of the vehicle velocity and orientation. An IMU measures linear acceleration and angular velocity in order to support inertial navigation in estimating (most commonly) position, velocity and attitude. This type of system is generally known as an inertial navigation system (INS).

The standard practice in inertial navigation is to measure the linear acceleration of the vehicle through the use of three accelerometers sensors, aligned orthogonally and mounted on the vehicle in a known position and orientation [8,41]. Similarly, angular velocity is measured by three gyroscope sensors, also aligned in order to provide orthogonal measurements and also mounted in a known position and orientation on the vehicle. In most cases, the three measurement axes are not oriented in a frame that is convenient for direct processing of the sensor measurements. Additionally, the origin of the measurement reference frame may be located at a point that is convenient for vehicle assembly, but provides little value for analysis of the measurements. Knowing the precise location and orientation of the IMU, relative to the vehicle, allows for the sensor measurements to be moved to a more appropriate position on the vehicle (such as the center of gravity or aerodynamic reference point), and transformed to a more significant reference frame (such as a body frame or aerodynamic frame). This

method of measurement post-processing provides an acceleration and angular rate output that can be readily used for onboard navigation or post-flight analysis.

In order to correctly apply the ADB reconstruction method, the readings from the accelerometer output must be understood. To be precise, an accelerometer measures the forces acting on the vehicle while excluding those forces acting on the sensor itself. In general, this means that the accelerometer output records the acceleration due to all of the forces acting on the vehicle, except for gravity. The accelerometer of a vehicle in free fall on a planetary body with no atmosphere (no drag forces), would, in theory, record acceleration values of exactly zero. In actuality for EDL trajectories, a number of forces could contribute to the reading of an accelerometer, including atmospheric drag, propulsive thrust, parachute drag, jettison events and surface impact.

In combination with the accelerometers on the IMU, the gyroscope sensors provide an output of angular velocity by sensing rotational changes experienced by the vehicle. The angular velocity measurements are used to determine the vehicle orientation, and are usually an important component of inertial navigation. While not explicitly used by the ADB algorithm, the angular velocity measurements are needed for inertial reconstruction, from which the a priori estimates of angle of attack and sideslip are obtained.

Recall that the ADB reconstruction algorithm relies on a comparison between the IMU measured accelerations and the force coefficients obtained from the aerodynamic database. In order for their comparison to be valid, they must describe the same forces. If the aerodynamic database produces force coefficients that reflect only the aerodynamic forces acting on the vehicle, those coefficients must be compared against accelerometer measurements for which the vehicle was under the influence of only aerodynamic forces. Conversely, if the acceleration measurements are taken during periods where non-aerodynamic forces were applied to the vehicle (for example, thrust or parachute drag force), the corresponding force coefficients must reflect those additional forces. More generally, the task of obtaining valid force coefficients for the ADB algorithm can be performed through the aerodynamic database alone when either (1) only aerodynamic forces are acting on the vehicle, or (2) the database has the ability to account for all non-aerodynamic forces acting on the vehicle. Otherwise, the force coefficients from the aerodynamic database must be augmented to account for non-aerodynamic forces, or that particular region of flight must be omitted from the reconstruction.

The need to appropriately compare acceleration measurements and force coefficients is an essential aspect of the ADB reconstruction. In some sense, it can be considered a limitation because it either adds complexity to the analysis or precludes its use during some portion of the trajectory. Yet because this reconstruction technique is best suited for EDL missions, as described in Chapter 2, it can be successfully applied over large ranges of flights for a variety of planetary entry missions. A majority of these missions have been flown ballistically (i.e. unguided), or with at least a portion of the trajectory subject to only aerodynamic deceleration. Furthermore, ballistic entry for EDL operations will continue to be utilized for future missions because the use of blunt body aeroshells to safely decelerate entry vehicles is still considered one of the most reliable and efficient methods currently available [42]. As such, the need to validly compare IMU measurements to aerodynamic database force coefficients does not pose a severe limitation when utilized for EDL missions. On the contrary, this requirement further supports the assertion that the ADB reconstruction method is well suited for EDL trajectories.

CHAPTER IV

ADB RECONSTRUCTION UNCERTAINTY ANALYSIS

An essential component to any reconstruction analysis is the assessment of uncertainty - a statistical characteristic of the state estimate. A statistical estimator, as its name suggests, utilizes the statistics of the process being modeled to update state variables in an optimal fashion [11]. In order to do so, these statistics, are tracked and updated internally by the estimator. As such, the use of statistical estimators for reconstruction provides a very convenient method of obtaining state uncertainties. Because of the deterministic nature of the ADB algorithm, a different method of uncertainty quantification must be applied to recover the accuracy of the reconstruction. For this research, an analytic method known as linear covariance mapping [43] is used to perform uncertainty assessment. The following sections derive the technique and describe the application of this uncertainty quantification method to the ADB reconstruction estimator.

4.1 Fundamentals of Linear Uncertainty Mapping

Uncertainty, also referred to as error, is a statistic that provides insight into the quality of an estimated parameter. The uncertainty of a parameter estimate can be qualitatively described as the accuracy to which the parameter is known as characterized by all of the factors that contribute to error in the estimate. Examples of uncertainty contributors include the accuracy or robustness of the analysis, the uncertainties associated with inputs to the analysis or any assumptions made in performing the analysis. In engineering, the error in an estimate is just as important to quantify as the parameter value because most mission or project requirements specify a desired accuracy for an analysis or at the very least, expect to know it. An analysis yielding low levels of uncertainty provides confidence in the results. Conversely, large uncertainties can also be informative by indicating a need to improve the analysis or mitigate the impact of the uncertainty elsewhere. Having a parameter estimate without its accuracy is of little value to an analyst.

Most quantitative measures of uncertainty describe the variability of a parameter. Variability is a statistical term that characterizes the spread or variation from the mean of the distribution of a random variable [44]. Some examples of variability

statistics include range, percentile, variance or standard deviation. Standard deviation (which is simply the square root of variance), is a commonly used metric for conveying parameter uncertainty and will be the metric chosen to describe the uncertainties associated with the ADB reconstruction outputs. For the rest of this thesis, the use of the term uncertainty will refer to standard deviation.

A statistical definition of standard deviation for a random sample of observations of the variable, θ, is defined by Eq. 25 [44].

$$\sigma = \sqrt{\frac{\sum_{i=1}^{n} \left(\theta_i - \bar{\theta}\right)^2}{N-1}} \tag{25}$$

In this equation, the standard deviation is calculated from a sample of N observations. Note that $\bar{\theta}$ is the mean value of θ from the sample of observations and σ is the standard deviation of θ. This definition of standard deviation is, in effect, an average of the deviations of each observation from the average of all of the observations in the sample. This definition also suggests that as the number of observations in the sample increases, the standard deviation of the random variable approaches zero. From a physical perspective, as the number of observations increases, the sample space approaches the actual population of the random variable, meaning that knowledge of the population is improving (and standard deviation is decreasing). If the sample covers the entire population, then the population is known exactly, and the standard deviation is equal to zero. As expressed by this definition, both mathematically and physically, the standard deviation of a parameter describes how well it is known.

For the ADB reconstruction algorithm, the approach taken to compute the standard deviations of reconstructed outputs is a form of uncertainty transformation derived from linearization of the reconstruction equations. This technique is an analytic method of recovering uncertainties by transforming (or propagating) the uncertainties of the analysis inputs into uncertainties around the analysis outputs [43]. The derivation of this technique will be described for any generic function, starting with a single input, single output function and expanded to include a function with any number of inputs. Consider the function z which has the output x and input θ:

$$x = z\left(\theta\right) \tag{26}$$

This function can be expanded using a Taylor series about the reference point, θ_0, as expressed by:

$$x = z\left(\theta\right) = z\left(\theta_0\right) + \frac{z_\theta\left(\theta_0\right)}{1!}\left(\theta - \theta_0\right) + \frac{z_{\theta\theta}\left(\theta_0\right)}{2!}\left(\theta - \theta_0\right)^2 + \frac{z_{\theta\theta\theta}\left(\theta_0\right)}{3!}\left(\theta - \theta_0\right)^3 + ... \tag{27}$$

In Eq. 27, $z_\theta(\theta_0)$ is the first derivative of z with respect to θ evaluated at the reference point, $z_{\theta\theta}(\theta_0)$ is the second derivative of z with respect to θ evaluated at the reference point, and so on. The form shown in the above equation provides three terms in the series, but implies that the expression continues with infinite terms. As the number of terms in the Taylor series advances, this approximation of the function becomes more accurate. A Taylor series expansion with an infinite number of terms represents the function exactly, provided that the function is infinitely differentiable about the reference point. A more concise definition of a Taylor series function representation is given by:

$$x = z(\theta) = \sum_{n=0}^{\infty} \frac{z_n(\theta_0)}{n!}(\theta - \theta_0)^n \tag{28}$$

where z_n is the nth order derivative of the function z. For the uncertainty mapping method to be used by the ADB reconstruction, the function is linearized by neglecting the second order and higher terms in the Taylor series expansion. For the generic function of Eq. 26, the first order linearization of the function becomes:

$$x = z(\theta) \approx z(\theta_0) + z_\theta(\theta_0)(\theta - \theta_0) \tag{29}$$

This expression is used directly to determine the covariance of the output, x, by taking the covariance of each side of the equation, and simplifying, as shown next:

$$\begin{aligned} \operatorname{cov}(x) &= \operatorname{cov}(z(\theta_0) + z_\theta(\theta_0)(\theta - \theta_0)) && (30) \\ \operatorname{cov}(x) &= \operatorname{cov}(z(\theta_0)) + \operatorname{cov}(z_\theta(\theta_0)(\theta - \theta_0)) && (31) \end{aligned}$$

The covariance of a constant variable is equal to zero, and the first term on the right hand side of Eq. 31 is eliminated.

$$\operatorname{cov}(x) = \operatorname{cov}(z_\theta(\theta_0)(\theta - \theta_0)) \tag{32}$$

Eq. 32 is then expanded, yielding the covariance of another constant variable, $-z_\theta(\theta_0)\theta_0$:

$$\begin{aligned} \operatorname{cov}(x) &= \operatorname{cov}(z_\theta(\theta_0)\theta - z_\theta(\theta_0)\theta_0) && (33) \\ \operatorname{cov}(x) &= \operatorname{cov}(z_\theta(\theta_0)\theta) + \operatorname{cov}(-z_\theta(\theta_0)\theta_0) && (34) \\ \operatorname{cov}(x) &= \operatorname{cov}(z_\theta(\theta_0)\theta) && (35) \end{aligned}$$

Next, Eq. 35 is simplified by applying the following rule when taking the covariance of a constant variable being multiplied by a random variable. In the following equation, a is a constant and θ is a random variable.

$$\operatorname{cov}(a\theta) = a^2 \operatorname{cov}(\theta) \tag{36}$$

After making use of the rule expressed in Eq. 36, Eq. 35 becomes:

$$\operatorname{cov}(x) = [z_\theta(\theta_0)]^2 \operatorname{cov}(\theta) \tag{37}$$

In this example, because the function input and output are single variables, the covariance of the input and output are equivalent to their variance. Eq. 37, can also be expressed as:

$$\sigma_x^2 = [z_\theta(\theta_0)]^2 \sigma_\theta^2 \tag{38}$$

This is also equivalent to:

$$\sigma_x^2 = \left(\frac{\partial z}{\partial \theta}\right)^2 \sigma_\theta^2 \tag{39}$$

$$\sigma_x = \sqrt{\left(\frac{\partial z}{\partial \theta}\right)^2 \sigma_\theta^2} = \left(\frac{\partial z}{\partial \theta}\right) \sigma_\theta \tag{40}$$

Eq. 40 is the general form for the uncertainty of the output to a single input, single output function based on linear mapping of uncertainty.

This result can be expanded to a more general case for functions with more than one input. Consider the function $\boldsymbol{z}$ which has the output x and the inputs θ and ϕ. The inputs can be noted in vector form by the vector $\boldsymbol{w}$ as shown by:

$$x = \boldsymbol{z}(\boldsymbol{w}) = \boldsymbol{z}(\theta, \phi) \tag{41}$$

As with the single input case, the derivation for uncertainty mapping for multiple inputs begins with a first order Taylor series expansion as expressed by:

$$x = \boldsymbol{z}(\theta, \phi) \approx \boldsymbol{z}(\theta_0, \phi_0) + \left[\frac{\partial \boldsymbol{z}}{\partial \theta}(\theta - \theta_0) + \frac{\partial \boldsymbol{z}}{\partial \phi}(\phi - \phi_0)\right] \tag{42}$$

Note that the partial derivative terms are evaluated at the reference condition $\boldsymbol{w}_0 = [\theta_0, \phi_0]$. In matrix form, Eq. 42 can be written as:

$$x = \boldsymbol{z}(\theta, \phi) \approx \boldsymbol{z}(\theta_0, \phi_0) + \begin{bmatrix} \frac{\partial \boldsymbol{z}}{\partial \theta} & \frac{\partial \boldsymbol{z}}{\partial \phi} \end{bmatrix} \begin{bmatrix} \theta - \theta_0 \\ \phi - \phi_0 \end{bmatrix} \tag{43}$$

This can also be written in terms of the input vector, $\boldsymbol{w}$:

$$x = \boldsymbol{z}(\boldsymbol{w}) \approx \boldsymbol{z}(\boldsymbol{w}_0) + \left[\frac{\partial \boldsymbol{z}}{\partial \boldsymbol{w}}\right] [\boldsymbol{w} - \boldsymbol{w}_0] \tag{44}$$

It is common to define the partial derivative of the function with respect to the function inputs as the Jacobian matrix, $\boldsymbol{J}$, such that Eq. 44 becomes:

$$x = \boldsymbol{z}(\boldsymbol{w}) \approx \boldsymbol{z}(\boldsymbol{w}_0) + \boldsymbol{J}[\boldsymbol{w} - \boldsymbol{w}_0] \tag{45}$$

Next, the covariance of Eq. 45 is applied as shown by:

$$\operatorname{cov}(x) = \operatorname{cov}(\boldsymbol{z}(\boldsymbol{w}_0) + \boldsymbol{J}[\boldsymbol{w} - \boldsymbol{w}_0]) \tag{46}$$

Simplifying Eq. 46, and noting that the covariance of a constant is equal to zero, yields:

$$\begin{aligned} \operatorname{cov}(x) &= \operatorname{cov}(\boldsymbol{z}(\boldsymbol{w}_0)) + \operatorname{cov}(\boldsymbol{J}[\boldsymbol{w} - \boldsymbol{w}_0]) && (47) \\ \operatorname{cov}(x) &= \operatorname{cov}(\boldsymbol{J}[\boldsymbol{w} - \boldsymbol{w}_0]) = \operatorname{cov}(\boldsymbol{J}\boldsymbol{w} - \boldsymbol{J}\boldsymbol{w}_0) && (48) \\ \operatorname{cov}(x) &= \operatorname{cov}(\boldsymbol{J}\boldsymbol{w}) + \operatorname{cov}(-\boldsymbol{J}\boldsymbol{w}_0) = \operatorname{cov}(\boldsymbol{J}\boldsymbol{w}) && (49) \end{aligned}$$

Then, using the rule expressed by Eq. 36 for taking the covariance of a constant quantity multiplied by a random variable, Eq. 49 becomes:

$$\operatorname{cov}(x) = \boldsymbol{J} \operatorname{cov}(\boldsymbol{w}) \boldsymbol{J}^T \tag{50}$$

Eq. 50 expresses the covariance of the output to the function $\boldsymbol{z}$, with input $\boldsymbol{w}$. For a single output, the covariance and variance of the output are equivalent. As such, Eq. 50 can also be written as:

$$\sigma_x^2 = \boldsymbol{J} \operatorname{cov}(\boldsymbol{w}) \boldsymbol{J}^T \tag{51}$$

Or, in terms of standard deviation, the uncertainty of the output variable can be expressed by:

$$\sigma_x = \sqrt{\boldsymbol{J} \operatorname{cov}(\boldsymbol{w}) \boldsymbol{J}^T} \tag{52}$$

For the example above, $\boldsymbol{z}$ is a function of only two inputs, but Eq. 52 is the general form of the transformation of uncertainty for any number of inputs. For functions having multiple inputs, the Jacobian matrix and the input covariance matrix must reflect the number of inputs. For example, a function with five inputs will have a Jacobian matrix that holds the partial derivative of the function with respect to all five inputs (a one by five matrix), and the input covariance matrix will carry the covariance elements for every input (a five by five matrix). This technique of uncertainty mapping using linearization will be applied to the ADB reconstruction method in order to estimate uncertainties on all of the reconstructed outputs.

4.2 Uncertainty Analysis Applied to ADB Reconstruction

As derived in Section 4.1, the uncertainties of estimated states computed by the ADB algorithm are obtained through a linear covariance mapping that transforms the input

uncertainties into output uncertainties. The general form of this transformation is expressed by:

$$\sigma_x = \sqrt{\boldsymbol{J}\,\mathrm{cov}\,(\boldsymbol{w})\,\boldsymbol{J}^T} \tag{53}$$

In order to generate uncertainties for each reconstructed state, Eq. 53 must be evaluated for each estimation equation. The covariance matrix of the inputs should be known before hand and the Jacobian matrix can be evaluated by taking the partial derivatives of the estimation equation with respect to the inputs. The following sections present the mathematical details of the uncertainty quantification method described in Section 4.1 as applied to the ADB reconstruction method. Section 4.2.1 provides the uncertainty assessment of air data states and Section 4.2.2 provides the uncertainty assessment of wind-relative attitude.

4.2.1 Uncertainty Assessment of Air Data States

The uncertainty assessment method detailed in Section 4.1 will first be applied to the air data states estimated in the outer loop of the ADB algorithm. The first reconstructed parameter is density, as expressed by:

$$\rho_k = -\frac{2ma_{x,k}}{{V_k}^2 SC_A} \tag{54}$$

First, the Jacobian matrix is evaluated by taking the partial derivatives of Eq. 54 with respect to each dependent variable. These partials with respect to m, a_x and S are shown in Eqs. 55-57:

$$\frac{\partial \rho_k}{\partial m} = -\frac{2a_{x,k}}{{V_k}^2 SC_A} \tag{55}$$

$$\frac{\partial \rho_k}{\partial a_{x,k}} = -\frac{2m}{{V_k}^2 SC_A} \tag{56}$$

$$\frac{\partial \rho_k}{\partial S} = \frac{2ma_{x,k}}{{V_k}^2 S^2 C_A} \tag{57}$$

Before evaluating the partials of the density equation with respect to velocity and axial force coefficient, an MSL-specific note must be made. For this uncertainty analysis, the aerodynamic force coefficients retrieved from the MSL aerodynamic database are assumed to be functions of velocity, Mach number and an uncertainty factor. The uncertainty factor is an input to the database that generates off-nominal static aerodynamic coefficients that reflect a specified level of uncertainty. This uncertainty is modeled through a set of adders and multipliers in both the hypersonic and supersonic regime that are applied to the nominal force coefficient value [45]. The aerodynamic

uncertainty values and the uncertainty model for MSL will be given in Section. 5.3, where all of the MSL input values are outlined. Thus, instead of differentiating the density equation with respect to the force coefficients, Eq. 54 is differentiated with respect to velocity, Mach number and uncertainty factor. The partial with respect to velocity can be derived analytically, as shown by Eq. 58:

$$\frac{\partial \rho_k}{\partial V_k} = \frac{2ma_{x,k}}{S}\left[\frac{V_k \frac{\partial C_A}{\partial V_k} - 2C_A}{{V_k}^3 C_A^2}\right] \tag{58}$$

In Eq. 58, the partial of C_A with respect to velocity is obtained numerically. Next, the partials with respect to Mach number and uncertainty factor can be obtained using the chain rule for differentiation as shown by Eqs. 59 and 60:

$$\frac{\partial \rho}{\partial M_k} = \frac{2ma_{x,k}}{SV_k^2 C_A^2}\frac{\partial C_A}{\partial M_k} \tag{59}$$

$$\frac{\partial \rho}{\partial \boldsymbol{u}} = \frac{2ma_{x,k}}{SV_k^2 C_A^2}\frac{\partial C_A}{\partial \boldsymbol{u}} \tag{60}$$

where $\boldsymbol{u}$ is a vector of uncertainty factor inputs composed of each element, adders and multipliers, of the uncertainty model. In the expressions above, the partials of C_A with respect to Mach number and uncertainty factor are computed numerically. Having evaluated these partial derivative expressions, the Jacobian matrix can be formed as such:

$$\boldsymbol{J}_{\rho_k} = \begin{bmatrix} \frac{\partial \rho_k}{\partial m} & \frac{\partial \rho_k}{\partial a_{x,k}} & \frac{\partial \rho_k}{\partial S} & \frac{\partial \rho_k}{\partial V_k} & \frac{\partial \rho_k}{\partial M_k} & \frac{\partial \rho_k}{\partial \boldsymbol{u}} \end{bmatrix} \tag{61}$$

Next, the variance and covariance values for the inputs to the estimation equation are used to assemble the covariance matrix of the inputs (where the input vector is defined as: $\boldsymbol{w}_\rho = [\ m \quad a_{x,k} \quad S \quad V_k \quad M_k \quad \boldsymbol{u}\ ]^T$):

$$\text{cov}\left(\boldsymbol{w}_\rho\right) = \begin{bmatrix} \sigma_m^2 & \lambda_{a_x,m} & \lambda_{S,m} & \lambda_{V_k,m} & \lambda_{M_k,m} & \lambda_{\boldsymbol{u},m} \\ \lambda_{m,a_x} & \sigma_{a_x}^2 & \lambda_{S,a_x} & \lambda_{V_k,a_x} & \lambda_{M_k,a_x} & \lambda_{\boldsymbol{u},a_x} \\ \lambda_{m,S} & \lambda_{a_x,S} & \sigma_S^2 & \lambda_{V_k,S} & \lambda_{M_k,S} & \lambda_{\boldsymbol{u},S} \\ \lambda_{m,V_k} & \lambda_{a_x,V_k} & \lambda_{S,V_k} & \sigma_{V_k}^2 & \lambda_{M_k,V_k} & \lambda_{\boldsymbol{u},V_k} \\ \lambda_{m,C_A} & \lambda_{a_x,C_A} & \lambda_{S,C_A} & \lambda_{V_k,C_A} & \sigma_{M_k}^2 & \lambda_{\boldsymbol{u},C_A} \\ \lambda_{m,\boldsymbol{u}} & \lambda_{a_x,\boldsymbol{u}} & \lambda_{S,\boldsymbol{u}} & \lambda_{V_k,\boldsymbol{u}} & \lambda_{M_k,\boldsymbol{u}} & \sigma_{\boldsymbol{u}^2} \end{bmatrix} \tag{62}$$

where $\lambda_{a_x,m}$ is the cross-covariance of inputs $a_{x,k}$ and m. The cross covariance of random variables A and B can be defined as:

$$\lambda_{A,B} = \rho_{A,B}\sigma_A\sigma_B \tag{63}$$

where $\rho_{A,B}$ is the correlation between A and B, and σ_A and σ_B are the standard deviations of A and B. If it is known or can be assumed that any of the inputs are uncorrelated, the corresponding off-diagonal covariance terms can be set equal to zero in the covariance matrix. It is important to note that this method of uncertainty assessment does not require uncorrelated inputs to the estimation equations, and if correlations between inputs are known to exist, they can easily be handled and mapped through the covariance transformation.

Finally, the uncertainty of the density estimate is computed by applying Eq. 61 and Eq. 62 to Eq. 53 as shown by:

$$\sigma_\rho^2 = \boldsymbol{J}_\rho \operatorname{cov}(\boldsymbol{w}_\rho)\boldsymbol{J}_\rho^T \tag{64}$$

The method detailed by Eqs. 54-64 is applied to each of the subsequent air data states computed in the ADB algorithm: pressure, speed of sound, Mach number, dynamic pressure and temperature. So as not to burden this section with lengthy partial derivative expressions, the equations for the Jacobian matrix of the other air data states are provided in Appendix B. The method exactly follows the derivation shown above for density using the unique estimation equations for pressure, speed of sound, Mach number and temperature.

4.2.2 Uncertainty Assessment of Wind Relative Attitude

The uncertainty mapping of the wind relative attitude is applied to the update equation derived in Section 3.1.2:

$$\begin{bmatrix}\alpha_{k,j}\\ \beta_{k,j}\end{bmatrix} = \begin{bmatrix}\alpha_{k,j-1}\\ \beta_{k,j-1}\end{bmatrix} - \begin{bmatrix}\frac{\partial f_1}{\partial \alpha_{k,j-1}} & \frac{\partial f_1}{\partial \beta_{k,j-1}}\\ \frac{\partial f_2}{\partial \alpha_{k,j-1}} & \frac{\partial f_2}{\partial \beta_{k,j-1}}\end{bmatrix}^{-1} \begin{bmatrix}\frac{C_{N,k,j-1}}{C_{A,k,j-1}} - \frac{a_{z,k}}{a_{x,k}}\\ \frac{C_{Y,k,j-1}}{C_{A,k,j-1}} + \frac{a_{y,k}}{a_{x,k}}\end{bmatrix} \tag{65}$$

For convenience, the variables q, r, s and t are substituted for the elements in the partial derivative matrix:

$$\begin{bmatrix}\alpha_{k,j}\\ \beta_{k,j}\end{bmatrix} = \begin{bmatrix}\alpha_{k,j-1}\\ \beta_{k,j-1}\end{bmatrix} - \begin{bmatrix}q & r\\ s & t\end{bmatrix} \begin{bmatrix}\frac{C_{N,k,j-1}}{C_{A,k,j-1}} - \frac{a_{z,k}}{a_{x,k}}\\ \frac{C_{Y,k,j-1}}{C_{A,k,j-1}} + \frac{a_{y,k}}{a_{x,k}}\end{bmatrix} \tag{66}$$

When taking the partial derivatives of Eq. 66, the elements of the partial derivative matrix are treated as constants. The update equation for angle of attack and angle of sideslip are treated separately in order to evaluate the uncertainties of each state. The scalar equation for each state update can be written as:

$$\alpha_{k,j} = \alpha_{k,j-1} - q\left(\frac{C_{N,k,j-1}}{C_{A,k,j-1}} - \frac{a_{z,k}}{a_{x,k}}\right) - r\left(\frac{C_{Y,k,j-1}}{C_{A,k,j-1}} + \frac{a_{y,k}}{a_{x,k}}\right) \tag{67}$$

$$\beta_{k,j} = \beta_{k,j-1} - s\left(\frac{C_{N,k,j-1}}{C_{A,k,j-1}} - \frac{a_{z,k}}{a_{x,k}}\right) - t\left(\frac{C_{Y,k,j-1}}{C_{A,k,j-1}} + \frac{a_{y,k}}{a_{x,k}}\right) \tag{68}$$

As was done for the uncertainty assessment of density shown in Section 4.2.1, the Jacobian matrix for angle of attack and sideslip are computed by taking the partial derivatives of their estimation equations with respect to the inputs. The uncertainty derivation for angle of attack will be treated first. The partial derivatives of Eq. 67 with respect to each of the inputs ($\alpha_{k,j-1}$, $C_{A,k,j-1}$, $C_{N,k,j-1}$, $C_{Y,k,j-1}$) will be computed. First, the partial derivative with respect to $\alpha_{k,j-1}$ is evaluated analytically:

$$\frac{\partial \alpha_{k,j}}{\partial \alpha_{k,j-1}} = 1 + q\frac{\partial}{\alpha_{k,j-1}}\left(\frac{C_{N,k,j-1}}{C_{A,k,j-1}}\right) - r\frac{\partial}{\alpha_{k,j-1}}\left(\frac{C_{Y,k,j-1}}{C_{A,k,j-1}}\right) \tag{69}$$

In Eq. 69, the partial derivative terms on the right hand side can be evaluated analytically using the quotient rule:

$$\frac{\partial}{\alpha_{k,j-1}}\left(\frac{C_{N,k,j-1}}{C_{A,k,j-1}}\right) = \frac{C_{A,k,j-1}\frac{\partial C_{N,k,j-1}}{\partial \alpha_{k,j-1}} - C_{N,k,j-1}\frac{\partial C_{A,k,j-1}}{\partial \alpha_{k,j-1}}}{C^2_{A,k,j-1}} \tag{70}$$

$$\frac{\partial}{\alpha_{k,j-1}}\left(\frac{C_{Y,k,j-1}}{C_{A,k,j-1}}\right) = \frac{C_{A,k,j-1}\frac{\partial C_{Y,k,j-1}}{\partial \alpha_{k,j-1}} - C_{Y,k,j-1}\frac{\partial C_{A,k,j-1}}{\partial \alpha_{k,j-1}}}{C^2_{A,k,j-1}} \tag{71}$$

In the above expressions, the partial derivatives of force coefficients with respect to $\alpha_{k,j-1}$ can be obtained numerically using the aerodynamic database. Next, instead of taking the partial derivatives with respect to the force coefficients, the partials of the angle of attack update equation are taken with respect to velocity, Mach number and uncertainty factor (as was done for the density equation) because of the assumed functional form of the force coefficients for the MSL aerodynamic database. The differentiation is performed through use of the chain rule as shown by Eqs. 72-74:

$$\frac{\partial \alpha_{k,j}}{\partial V_k} = \frac{\partial \alpha_{k,j}}{\partial C_{A,k,j-1}}\frac{\partial C_{A,k,j-1}}{\partial V_k} + \frac{\partial \alpha_{k,j}}{\partial C_{N,k,j-1}}\frac{\partial C_{N,k,j-1}}{\partial V_k} + \frac{\partial \alpha_{k,j}}{\partial C_{Y,k,j-1}}\frac{\partial C_{Y,k,j-1}}{\partial V_k} \tag{72}$$

$$\frac{\partial \alpha_{k,j}}{\partial M_k} = \frac{\partial \alpha_{k,j}}{\partial C_{A,k,j-1}}\frac{\partial C_{A,k,j-1}}{\partial M_k} + \frac{\partial \alpha_{k,j}}{\partial C_{N,k,j-1}}\frac{\partial C_{N,k,j-1}}{\partial M_k} + \frac{\partial \alpha_{k,j}}{\partial C_{Y,k,j-1}}\frac{\partial C_{Y,k,j-1}}{\partial M_k} \tag{73}$$

$$\frac{\partial \alpha_{k,j}}{\partial \boldsymbol{u}} = \frac{\partial \alpha_{k,j}}{\partial C_{A,k,j-1}}\frac{\partial C_{A,k,j-1}}{\partial \boldsymbol{u}} + \frac{\partial \alpha_{k,j}}{\partial C_{N,k,j-1}}\frac{\partial C_{N,k,j-1}}{\partial \boldsymbol{u}} + \frac{\partial \alpha_{k,j}}{\partial C_{Y,k,j-1}}\frac{\partial C_{Y,k,j-1}}{\partial \boldsymbol{u}} \tag{74}$$

The partial derivatives of each force coefficient with respect to velocity, Mach number and uncertainty factor must be computed numerically. The partial derivatives of α_j with respect to each force coefficient can be computed analytically as given by the following expressions:

$$\frac{\partial \alpha_{k,j}}{\partial C_{A,k,j-1}} = -q\frac{C_{N,k,j-1}}{C^2_{A,k,j-1}} + r\frac{C_{Y,k,j-1}}{C^2_{A,k,j-1}} \tag{75}$$

$$\frac{\partial \alpha_{k,j}}{\partial C_{N,k,j-1}} = \frac{q}{C_{A,k,j-1}} \tag{76}$$

$$\frac{\partial \alpha_{k,j}}{\partial C_{Y,k,j-1}} = -\frac{r}{C_{A,k,j-1}} \tag{77}$$

Having evaluated the partial derivatives of the update equation, the Jacobian matrix is assembled in the following form:

$$\boldsymbol{J}_{\alpha_{k,j}} = \begin{bmatrix} \frac{\partial \alpha_{k,j}}{\partial \alpha_{k,j-1}} & \frac{\partial \alpha_{k,j}}{\partial V_k} & \frac{\partial \alpha_{k,j}}{\partial M_k} & \frac{\partial \alpha_{k,j}}{\partial \boldsymbol{u}} \end{bmatrix} \tag{78}$$

Next, the covariance of the inputs is assembled as given by:

$$\operatorname{cov}\left(\boldsymbol{w}_{\alpha_{k,j}}\right) = \begin{bmatrix} \sigma^2_{\alpha_{k,j-1}} & \lambda_{V_k,\alpha_{k,j-1}} & \lambda_{M_k,\alpha_{k,j-1}} & \lambda_{\boldsymbol{u},\alpha_{k,j-1}} \\ \lambda_{\alpha_{k,j-1},V_k} & \sigma^2_{V_k} & \lambda_{M_k,V_k} & \lambda_{\boldsymbol{u},V_k} \\ \lambda_{\alpha_{k,j-1},M_k} & \lambda_{V_k,M_k} & \sigma^2_{M_k} & \lambda_{\boldsymbol{u},M_k} \\ \lambda_{\alpha_{k,j-1},\boldsymbol{u}} & \lambda_{V_k,\boldsymbol{u}} & \lambda_{M_k,\boldsymbol{u}} & \sigma^2_{\boldsymbol{u}} \end{bmatrix} \tag{79}$$

Finally, the uncertainty of angle of attack can be computed by substituting Eq. 78 and Eq. 79 into Eq. 53 as expressed by:

$$\sigma_{\alpha_{k,j}} = \sqrt{\boldsymbol{J}_{\alpha_{k,j}} \operatorname{cov}\left(\boldsymbol{w}_{\alpha_{k,j}}\right) \boldsymbol{J}^T_{\alpha_{k,j}}} \tag{80}$$

The procedure completed in Eqs. 69-80 is repeated for the angle of sideslip equation. The partial derivatives of Eq. 68 with respect to the inputs are:

$$\frac{\partial \beta_{k,j}}{\partial \beta_{k,j-1}} = 1 + s\frac{\partial}{\beta_{k,j-1}}\left(\frac{C_{N,k,j-1}}{C_{A,k,j-1}}\right) - t\frac{\partial}{\beta_{k,j-1}}\left(\frac{C_{Y,k,j-1}}{C_{A,k,j-1}}\right) \tag{81}$$

$$\frac{\partial \beta_{k,j}}{\partial V_k} = \frac{\partial \beta_{k,j}}{\partial C_{A,k,j-1}}\frac{\partial C_{A,k,j-1}}{\partial V_k} + \frac{\partial \beta_{k,j}}{\partial C_{N,k,j-1}}\frac{\partial C_{N,k,j-1}}{\partial V_k} + \frac{\partial \beta_{k,j}}{\partial C_{Y,k,j-1}}\frac{\partial C_{Y,k,j-1}}{\partial V_k} \tag{82}$$

$$\frac{\partial \beta_{k,j}}{\partial M_k} = \frac{\partial \beta_{k,j}}{\partial C_{A,k,j-1}}\frac{\partial C_{A,k,j-1}}{\partial M_k} + \frac{\partial \beta_{k,j}}{\partial C_{N,k,j-1}}\frac{\partial C_{N,k,j-1}}{\partial M_k} + \frac{\partial \beta_{k,j}}{\partial C_{Y,k,j-1}}\frac{\partial C_{Y,k,j-1}}{\partial M_k} \tag{83}$$

$$\frac{\partial \beta_{k,j}}{\partial \boldsymbol{u}} = \frac{\partial \beta_{k,j}}{\partial C_{A,k,j-1}}\frac{\partial C_{A,k,j-1}}{\partial \boldsymbol{u}} + \frac{\partial \beta_{k,j}}{\partial C_{N,k,j-1}}\frac{\partial C_{N,k,j-1}}{\partial \boldsymbol{u}} + \frac{\partial \beta_{j}}{\partial C_{Y,k,j-1}}\frac{\partial C_{Y,k,j-1}}{\partial \boldsymbol{u}} \tag{84}$$

The partial derivative terms on the right hand side of Eq. 81 can be evaluated analytically using the quotient rule:

$$\frac{\partial}{\beta_{k,j-1}}\left(\frac{C_{N,k,j-1}}{C_{A,k,j-1}}\right) = \frac{C_{A,k,j-1}\frac{\partial C_{N,k,j-1}}{\partial \beta_{k,j-1}} - C_{N,k,j-1}\frac{\partial C_{A,k,j-1}}{\partial \beta_{j-1}}}{C^2_{A,k,j-1}} \tag{85}$$

$$\frac{\partial}{\beta_{k,j-1}}\left(\frac{C_{Y,k,j-1}}{C_{A,k,j-1}}\right) = \frac{C_{A,k,j-1}\frac{\partial C_{Y,k,j-1}}{\beta_{k,j-1}} - C_{Y,k,j-1}\frac{\partial C_{A,k,j-1}}{\partial \beta_{k,j-1}}}{C^2_{A,k,j-1}} \tag{86}$$

The partial derivative terms of $\beta_{k,j}$ with respect to the force coefficients in Eqs. 82-84 can be computed analytically from the following equations:

$$\frac{\partial \beta_{k,j}}{\partial C_{A,k,j-1}} = -\frac{t}{C_{A,k,j-1}} \tag{87}$$

$$\frac{\partial \beta_{k,j}}{\partial C_{N,k,j-1}} = \frac{s}{C_{A,k,j-1}} \tag{88}$$

$$\frac{\partial \beta_{k,j}}{\partial C_{Y,k,j-1}} = -s\frac{C_{N,k,j-1}}{C^2_{A,k,j-1}} + t\frac{C_{Y,k,j-1}}{C^2_{A,k,j-1}} \tag{89}$$

As was done for the angle of attack uncertainty, the angle of sideslip Jacobian matrix and input covariance can be evaluated, shown by Eq. 90 and Eq. 91:

$$\boldsymbol{J}_{\beta_{k,j}} = \begin{bmatrix} \frac{\partial \beta_{k,j}}{\partial \beta_{k,j-1}} & \frac{\partial \beta_{k,j}}{\partial V_k} & \frac{\partial \beta_{k,j}}{\partial M_k} & \frac{\partial \beta_{k,j}}{\partial \boldsymbol{u}} \end{bmatrix} \tag{90}$$

$$\operatorname{cov}\left(\boldsymbol{w}_{\beta_{k,j}}\right) = \begin{bmatrix} \sigma^2_{\beta_{k,j-1}} & \lambda_{V_k,\beta_{k,j-1}} & \lambda_{M_k,\beta_{k,j-1}} & \lambda_{\boldsymbol{u},\beta_{k,j-1}} \\ \lambda_{\beta_{k,j-1},V_k} & \sigma^2_{V_k} & \lambda_{M_k,V_k} & \lambda_{\boldsymbol{u},V_k} \\ \lambda_{\beta_{k,j-1},M_k} & \lambda_{V_k,M_k} & \sigma^2_{M_k} & \lambda_{\boldsymbol{u},M_k} \\ \lambda_{\beta_{k,j-1},\boldsymbol{u}} & \lambda_{V_k,\boldsymbol{u}} & \lambda_{M_k,\boldsymbol{u}} & \sigma^2_{\boldsymbol{u}} \end{bmatrix} \tag{91}$$

Finally, the uncertainty of angle of sideslip can be expressed using the linear uncertainty mapping equation by substituting the corresponding Jacobian and input covariance terms:

$$\sigma_{\beta_{k,j}} = \sqrt{\boldsymbol{J}_{\beta_{k,j}} \operatorname{cov}\left(\boldsymbol{w}_{\beta_{k,j}}\right) \boldsymbol{J}^T_{\beta_{k,j}}} \tag{92}$$

CHAPTER V

APPLICATION OF THE ADB RECONSTRUCTION TO MSL

This chapter presents an outline of the MSL EDL mission to provide some context regarding the application of the ADB reconstruction method. The entry trajectory is described and the region of the trajectory best suited for the ADB algorithm is highlighted. The input data used for the MSL reconstruction and uncertainty assessment are detailed.

5.1 MSL EDL Overview

On August 5th, 2012 the MSL entry vehicle successfully entered the Martian atmosphere and delivered the Curiosity rover safely to the surface of the planet. The primary goal of the MSL EDL mission was to safely land the rover at a location known as Gale Crater. During EDL, measurement instrumentation onboard the entry vehicle was used to collect various forms of data for real-time processing and post-flight analysis. Examples of measurement sensors used by the MSL vehicle include accelerometers and gyroscopes (used as part of an IMU), pressure transducers (used as part of a Flush Air Data System), thermocouples, recession sensors, and radar altimeters. Each measurement system provided information regarding the state of the vehicle during entry. The measurements were used, and often combined, for various post-flight analyses, including trajectory reconstruction. As described in Chapter 3, the ADB reconstruction algorithm relies only on the measurements recorded by the IMU in order to reconstruct air data states and wind-relative attitude.

The MSL EDL mission, depicted by Fig. 11, consisted of six main segments: exo-atmospheric, entry, parachute descent, powered descent, sky crane and flyaway [46]. During the exo-atmospheric portion of flight, the cruise stage was separated from the vehicle, and Guidance, Navigation and Control (GNC) was enabled. The vehicle was then de-spun and set to its entry orientation. Two Cruise Balance Masses (CBMs), each 75 kg, were jettisoned, inducing a center of mass offset that allowed the vehicle to generate aerodynamic lift.

Next, the vehicle Entry Interface Point (EIP) was reached at an aerocentric radius of 3522.2 km, approximately 540 seconds after cruise stage separation. During entry,

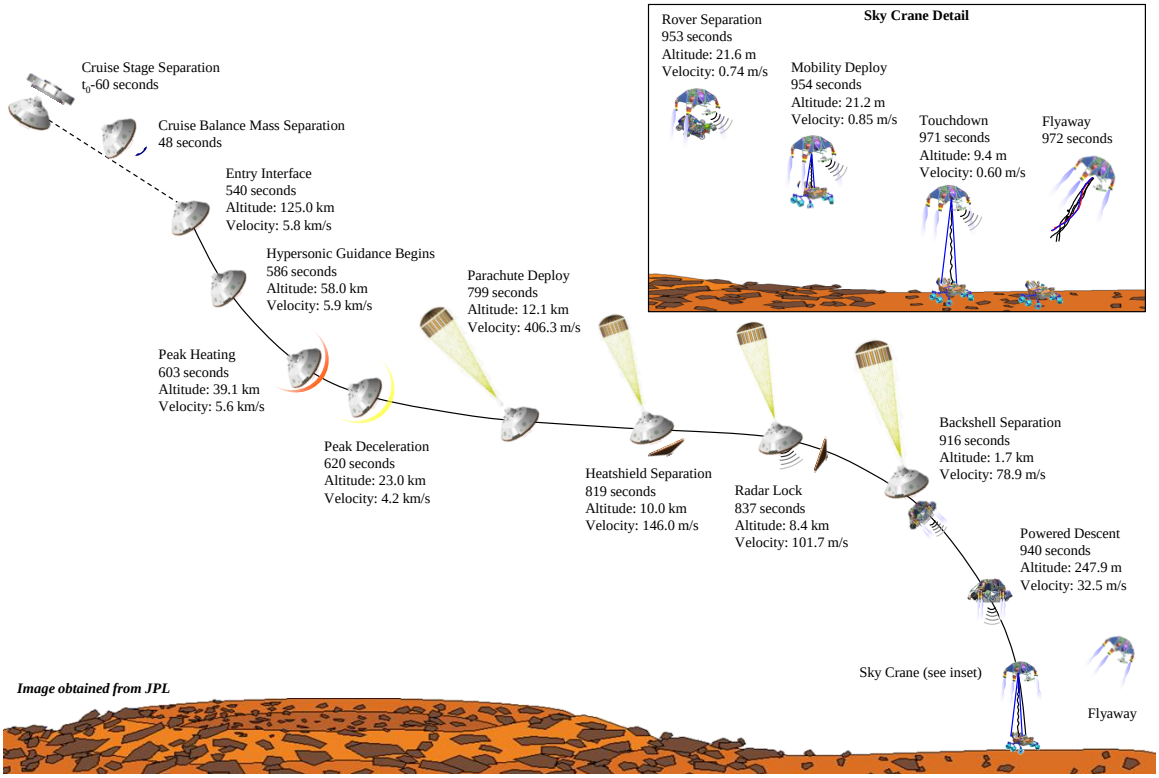

Figure 11: MSL EDL Mission Overview

the lift vector of the vehicle was manipulated through a reaction control system (RCS), in order to attain the desired down-range and cross-range targets. Additionally, control of the lift vector was used to produce a series of bank maneuvers (also referred to as bank reversals), removing energy from the vehicle and allowing it to reach the velocity required for parachute deployment. The vehicle experienced peak heating and peak deceleration during the entry phase of the trajectory. Just prior to parachute deployment, six 25 kg Entry Balance Masses (EBMs) were jettisoned, eliminating the center of mass offset and, consequently, any lift generated by the vehicle. The final maneuver during the entry phase was to roll the vehicle in order to point its radar altimeter sensors in the direction of the planet's surface in preparation for parachute deployment. This maneuver is referred to as the Straighten Up and Fly Right (SUFR) maneuver. Note that the entry segment of the mission lacked the use of a parachute and was limited propulsively to RCS firings. Because the forces acting on the vehicle were predominantly aerodynamic, the ADB reconstruction method was applied during this segment. This will be described in more detail in Section 5.2.

The next two segments of the trajectory, parachute descent and powered descent, shifted the approach used to slow the vehicle from aerodynamic to a more active form

of deceleration. The start of the parachute descent phase coincided with parachute deployment which was triggered at a Mach number of 1.7. The heat shield was jettisoned at Mach 0.7, allowing the radar altimeters (to this point protected by the heat shield) to begin acquiring the ground. The backshell, to which the parachute was attached, was jettisoned at an altitude of 1.6 km and a velocity of 79 m/s. At this point, the powered descent phase of the trajectory was initiated and eight Mars Landing Engines (MLEs) were engaged to complete the entry segment of the trajectory. The MLEs, capable of independent throttling, were used to achieve vertical flight with a constant descent rate of 32 m/s. A constant deceleration phase followed, reducing the vehicle speed to 0.75 m/s in preparation for landing. The landing phase

Table 2: MSL EDL Timeline

Event	Time (s)
Entry Interface	540.00
Guidance Start	585.88
Bank Reversal 1	612.88
Peak Deceleration	620.33
Bank Reversal 2	633.88
Bank Reversal 3	663.38
Heading Alignment	675.63
EBM Jettison	779.87
Parachute Deployment	799.12
Heat shield Separation	818.87
Radar Lock	837.12
Prime MLE Rockets	899.63
Backshell Separation	915.92
Powered Approach	918.38
Skycrane Start	952.89
Ready for Touchdown	961.86
Touchdown Sensed	971.52
Fly Away	972.31

of the trajectory consisted of two complex maneuvers: sky crane and fly away. The sky crane segment began at approximately 18.6 m, following issuance of the rover separation command. The rover, still attached to the descent stage by a bridle and electrical umbilical, was lowered to a position of 7.5 m below the descent stage. Once this position was reached, the descent stage and suspended rover descended together until touchdown was detected. The flyaway segment followed by severing the bridle and umbilical, and throttling the MLEs to send the descent stage a safe distance

away from the rover. At this point, with the rover safely on the surface of Mars, the EDL mission was complete. A timeline of the events occurring during the MSL EDL mission is given in Table 2. Note that the times listed in the table are with respect to the number of seconds past cruise stage separation.

5.2 MSL Applicable Trajectory

When applying the ADB reconstruction method, it is important to identify the areas of the trajectory where the algorithm would provide valid and accurate results. As discussed in Chapter 3, this is done by recognizing the forces acting on the vehicle during the reconstructed portion of the trajectory. During the entry phase of the trajectory, only aerodynamic and propulsive forces were acting on the vehicle. Propulsive forces were applied by the RCS for attitude control in directing specific orientations or initiating maneuvers. For many portions of the entry phase, the RCS thrusters were sparsely actuated or not engaged at all, providing significant areas of the trajectory well suited for ADB reconstruction.

The regions during the entry segment when thrust was commanded by the flight software are presented in Fig. 12. The grey, shaded regions denote those portions of the trajectory where the RCS was engaged and white regions denote portions where only aerodynamic forces were affecting the vehicle dynamics (referred to as quiescent periods). These regions are shown alongside an estimate of Mach number in order to provide context, and labels are shown to indicate the start of events that reflect prolonged thruster firing. It is clear from the figure that a majority of this period is quiescent, and that RCS firings (which were found to exist in 24.6% of the data points during this region) are only prominent during dynamic maneuvers. Specifically, the three bank reversals used to reduce entry velocity can be identified based on thruster firing history. The first reversal occurs between (approximately) 612 and 625 seconds, the second between 633 and 645 seconds, and the third between 663 and 685 seconds. In addition to the bank reversals, two prolonged periods of RCS activity were observed between 780 and 800 seconds. These firings were commanded to damp angular rates during the SUFR maneuver, with each period lasting for approximately six or seven seconds.

The ADB reconstruction is performed on the MSL trajectory between 600 and 800 seconds. Before 600 seconds, the atmosphere through which the entry vehicle flew lacked sufficient density to perform the ADB reconstruction. In this thinner region of the atmosphere, the aerodynamic forces measured by the accelerometer are too small

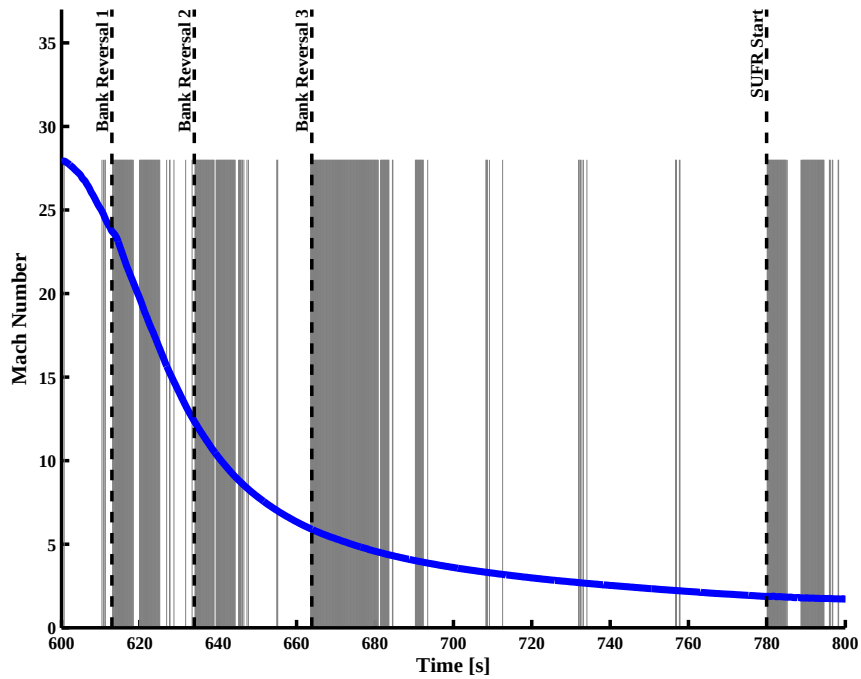

Figure 12: MSL RCS Firings During Entry

to distinguish from the sensor noise, and distinct dynamics become very difficult to identify even after utilization of filtering techniques. As such, the reconstruction before 600 seconds yields excessively noisy state estimates from the ADB algorithm. At 799 seconds, the parachute is deployed and the parachute drag force becomes a significant contributor to the overall force experienced by the vehicle. Beyond 800 seconds, the ADB reconstruction method can no longer be used. In spite of these limitations, the 200 second portion of the trajectory selected for reconstruction represents a significant region of flight during entry. The ADB reconstruction was successfully applied to this region, and the results are presented in Chapter 6.

5.3 ADB Reconstruction Inputs for MSL

The ADB reconstruction algorithm requires the following inputs for estimation of output states:

- axial, side and normal body acceleration at the center of gravity (CG)
- altitude
- velocity
- local acceleration due to gravity

- vehicle reference area, S
- vehicle mass, m
- ratio of specific heats, γ
- gas constant of atmosphere, R

For application to the MSL flight data, the accelerations are obtained from the onboard IMU, and transformed to the CG location. Altitude and velocity are obtained through an inertial reconstruction. The vehicle mass profile is obtained through a post-flight mass properties reconstruction [47] performed by the Jet Propulsion Laboratory (JPL). The local acceleration due to gravity is computed at each time based on the inertially reconstructed altitude using Eq. 6. Finally, reference area [48], ratio of specific heats and atmospheric gas constant are properties know pre-flight and assumed to be constant. The acceleration signals used by the ADB reconstruction are shown in Figure 13. A running mean smoother with a window size of 1.335 seconds is applied to the accelerations in order to remove measurement noise and produce smoothed reconstructed states. The window size corresponds to 89 frames of the IMU data, which was obtained at 66 Hz. The altitude and velocity profiles are shown in Fig. 14 and the entry mass profile is presented in Fig. 15. The values used for reference area, ratio of specific heats and atmospheric gas constant are given in Table 3.

Table 3: MSL Constant Input Values

Parameter	Value
Reference Area, S	16.04 m^2
Ratio of Specific Heats, γ	1.335
Gas Constant, R	188.92 J/kg/K

The entry vehicle aerodynamics, a critical component to the ADB reconstruction approach, are obtained from the MSL aerodynamic database. This database was characterized through a combination of computational fluid dynamics (CFD) code and wind tunnel testing. Specifically, the Langley Aerothermodynamics Upwind Relaxation Algorithm (LAURA) CFD code, and measurements from the Langley Unitary Plan Wind Tunnel (UPWT) and the Langley 31" Mach 10 Hypersonic Tunnel were used to formulate the flight aerodynamic database for the hypersonic and supersonic

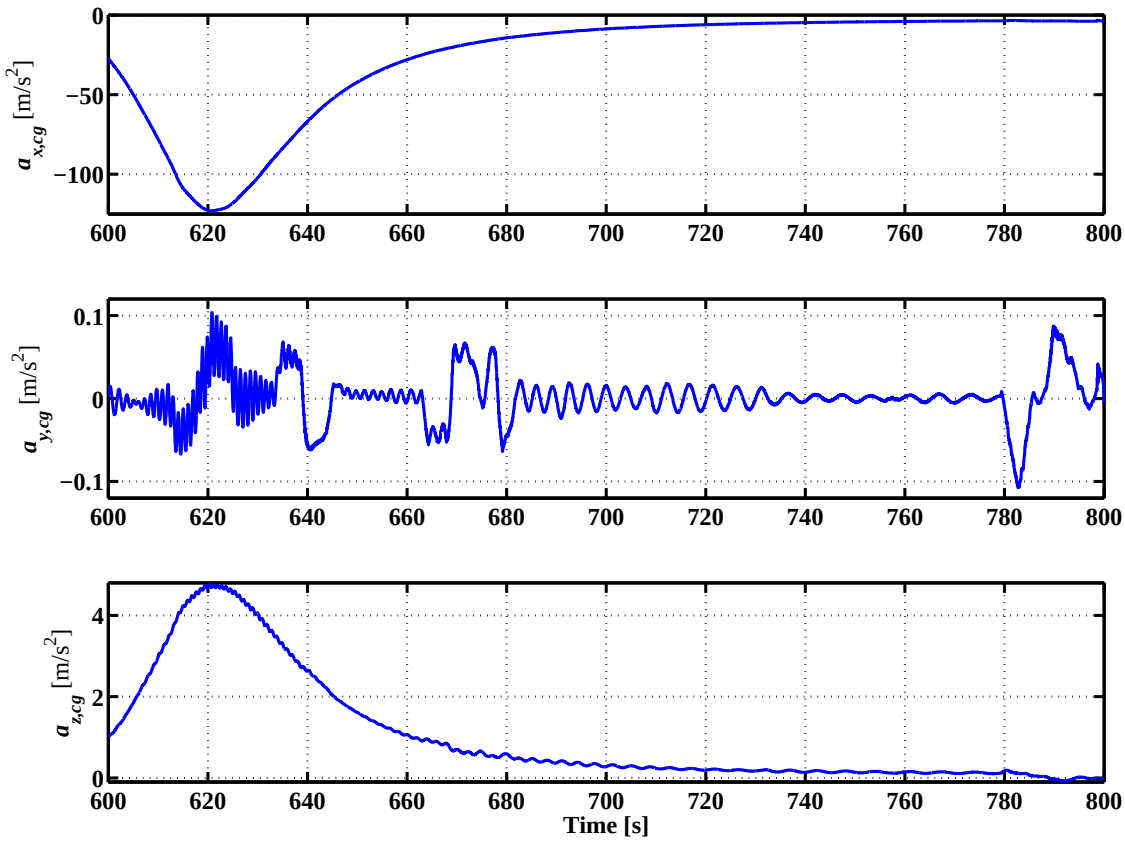

Figure 13: MSL Body Acceleration Signals

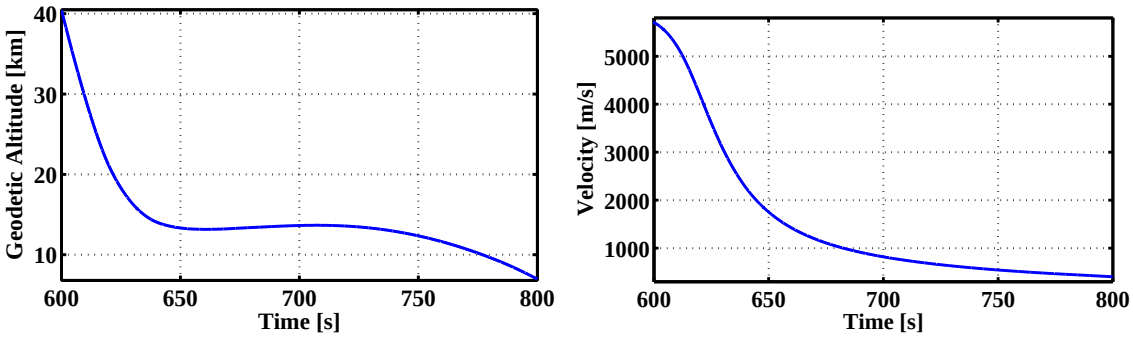

(a) Geodetic Altitude (b) Velocity Magnitude

Figure 14: MSL Altitude and Velocity

regimes experienced during flight [45]. Reference [45] provides further details on the MSL aerodynamics and the development of the aerodynamic database. For the MSL vehicle, the driving inputs in retrieving force coefficients from the aerodynamic database are angle of attack, angle of sideslip and Mach number. In fact, the derivation of the ADB method presented here is based on this functional form. While this

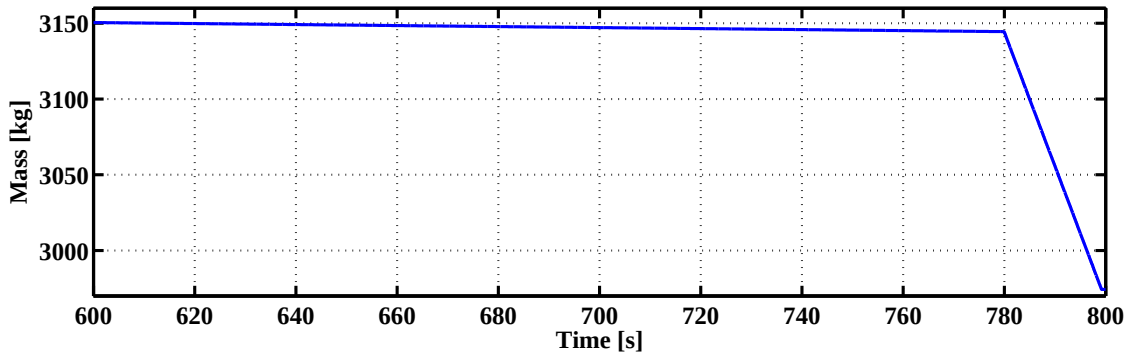

Figure 15: MSL mass profile

set of inputs is very common for an aerodynamic database, the ADB method would require modification for a database whose inputs were different than that of MSL.

Another MSL-specific note should be made here on the ADB uncertainty assessment. Most of the cross-covariance terms in the input covariance matrices (as described in Section 4.2) are assumed to equal zero. In general this is a valid assumption, as most of the inputs do not share correlations. It was found that this assumption is not valid for the cross-covariance of altitude at the current time, r_k, and altitude at the previous time, r_{k-1}, used in the estimation of pressure uncertainty. By matching the uncertainties derived from a Monte Carlo analysis of the MSL trajectory, the correlation between these two terms was identified to be very high, at a value of approximately 0.97. This is the only place in the uncertainty assessment where a correlation is required, and correlations between all other inputs are assumed equal to zero. Identifying correlations using an analytical method is an item requiring further attention and will be considered in future work.

Because the uncertainty assessment for the ADB reconstruction maps input uncertainties to output variances, the uncertainty of each input must be known. The acceleration uncertainties are generated based on the accelerometer accuracy specifications given in Table 4 [49]. Note that the noise error values refer to the smoothed acceleration signals computed by the running mean. The noise error values in Table 4 were obtained by applying the smoother to simulated MSL acceleration data carrying noise from an IMU model. The simulated data were smoothed and compared to the known truth data in order estimate the remaining noise content. Thus, the noise error values used to compute the acceleration uncertainties more closely represent the true signal noise after application of the running mean smoother. The resulting acceleration 1-σ uncertainty profiles are given in Fig. 16.

Table 4: MSL IMU Accelerometer Error Parameters

Error Parameter	Value (3-σ)
Misalignment	0.05 deg
Noise, x-axis	13.57 mg
Noise, y/z-axis	2.58 mg
Scale Factor	450 ppm
Bias	100 μg

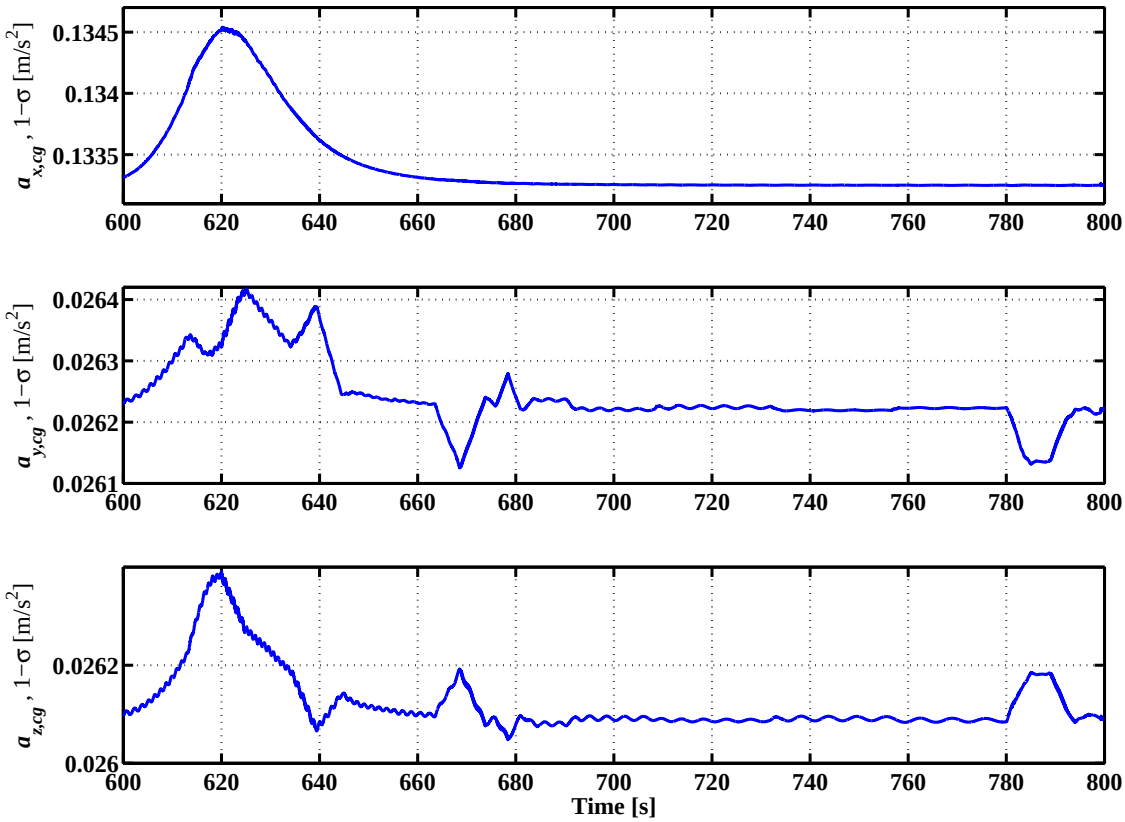

Figure 16: MSL Body Acceleration Uncertainties

The altitude and velocity uncertainties, shown in Fig. 17, are obtained through covariance propagation as described in Section 1.2.

The mass uncertainty is obtained from an MSL mass properties assessment, given in Ref. [47]. Reference area uncertainty is obtained from pre-flight laser scan measurements of the heat shield, documented in Ref. [50]. Lastly, gravity uncertainty is based on the assumed gravity model used in the analysis that neglects perturbation effects. Exclusion of the dominant perturbation, the zonal J_2 harmonic, results in a relatively small error, on the order of one third of a percent [38]. Additionally, uncertainty in

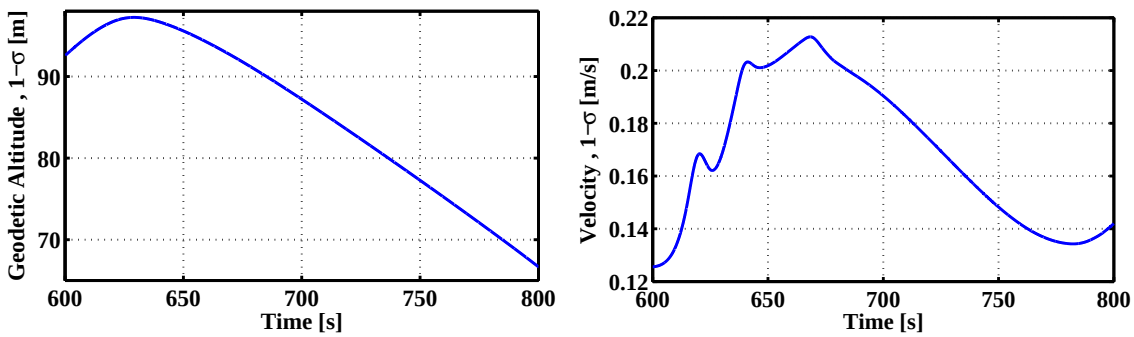

(a) Geodetic Altitude

(b) Velocity Magnitude

Figure 17: MSL Altitude and Velocity Uncertainties

the vehicle aerocentric radius would also contribute to the gravity uncertainty. The radius uncertainty obtained from inertial reconstruction varies between 0.2% and 1% through the trajectory. Based on these findings, an assumed value of 1% is used for gravity uncertainty. This is considered a conservative estimate, but as will be shown in Section 6.3, gravity uncertainty is not a large contributor to the uncertainty estimates of free-stream pressure. The mass, reference area and gravity uncertainties are summarized in Table 5.

Table 5: MSL Constant Input Uncertainties

Error Parameter	Value (1-σ)
Mass	5.33 kg
Gravity	1%
Reference Area	2.366E-3 m^2

The uncertainty of each force coefficient is modeled through a set of uncertainty factors that are provided to the aerodynamic database to disperse the static aerodynamics of the vehicle or account for off-nominal aerodynamic behavior. The uncertainty factors are a set of adders and multipliers applied to the nominal coefficient inside of the database. The resulting dispersed force coefficients reflect the aerodynamic uncertainty values (3-σ) given in Ref. [45], shown in Table 6.

The uncertainty models for each coefficient are given by Eqs. 93-95, where unique uncertainty factor values are used in the hypersonic and supersonic regime, reflecting the MSL aerodynamic uncertainties given in Table 6. Note that the uncertainty between the two regimes is linearly blended [45].

Table 6: MSL 3-σ Static Aerodynamic Uncertainties

Flight Regime	C_A	C_N	C_Y
Mach > 10	±3%	±0.01	±10%
Mach < 5	±10%	±0.01	±10%

$$C_{A,Disp} = C_{A,Nom}\left(1 + U^M_{C_A}\right) \tag{93}$$

$$C_{N,Disp} = \left[C_{N,Nom} + U^A_{C_N}\right]\left(1 + U^M_{C_N}\right) \tag{94}$$

$$C_{Y,Disp} = C_{Y,Nom} + U^A_{C_Y} \tag{95}$$

In the equations above, $U^M_{C_x}$ is the uncertainty multiplier and $U^A_{C_x}$ is the uncertainty adder [45]. The subscripts '$Disp$' and 'Nom' refer to the dispersed and nominal aerodynamic coefficients, respectively.

CHAPTER VI

RECONSTRUCTION RESULTS

In this chapter the results of the ADB reconstruction method as applied to the MSL EDL flight data are presented. The performance of the ADB reconstruction is assessed through comparison against the extended Kalman filter (EKF) and inertial reconstructions performed by the Mars Entry, Descent and Landing Instrumentation (MEDLI) team [13]. The EKF reconstruction is an optimal estimate of reconstructed outputs that leverages multiple sources of flight data taken during entry. These data sources include the acceleration and angular velocity measurements from the IMU, pressure measurements from heat shield pressure transducers, slant range and range rate measurements from the radar altimeter, and the landing site location based on camera images taken by the MSL descent stage. In addition to the flight data measurements, a mesoscale atmosphere model derived post-flight is utilized by the EKF to provide measurements of the atmosphere. The determination of the mesoscale atmosphere model is described in Ref. [51]. Details of the methodology used by the EKF and inertial reconstructions can be found in Refs. [13] and [10]. The ADB reconstruction uncertainties are also examined to assess the accuracy of the algorithm in estimating all of the output parameters. Lastly, a sensitivity analysis is performed in order to characterize the contributions of each input to the output uncertainties.

6.1 MSL State Reconstructions

The estimates of atmosphere and air data states (density, dynamic pressure, static pressure, temperature and Mach number) reconstructed by the ADB, EKF and inertial reconstructions are presented in Figs. 18-19. The ADB reconstruction is shown by the black, solid line, the EKF reconstruction is shown by the dashed, red line, and the inertial reconstruction is shown by the dashed, blue line. The mesoscale atmosphere model used as an observation inside of the EKF is also shown (by a dashed, green line) for the comparisons of atmosphere. On each plot, grey shaded regions are used to denote areas where RCS thruster firings were recorded by the entry vehicle flight software. These regions indicate sections of the reconstruction where the ADB method may differ from the EKF reconstruction as non-aerodynamic forces were affecting the vehicle dynamics.

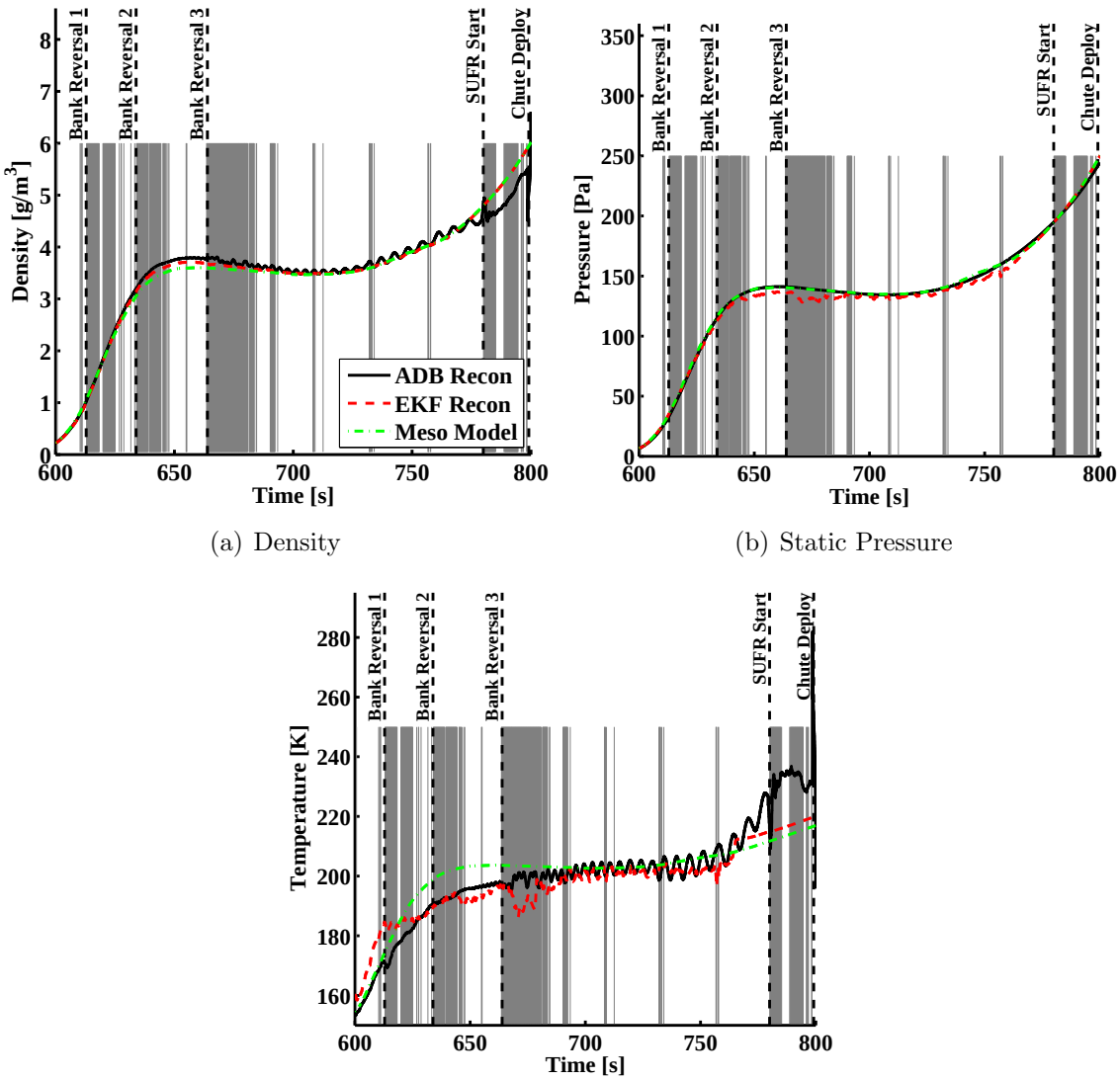

(a) Density

(b) Static Pressure

(c) Temperature

Figure 18: Atmosphere State Estimates

The ADB reconstruction results of the atmosphere states are in good agreement with the EKF reconstruction and mesoscale model. All three atmosphere states are within 5% of the EKF values for most of the trajectory. Between 600 and 780 seconds the ADB density deviates from the EKF density by approximately 1% to 4%. Pressure deviations are on the order of 2% to 10% with a maximum difference of roughly 12 Pa. Temperature differences vary between 2% and 10% with maximum temperature differences on the order of 15 K. Oscillations in the reconstructed atmosphere states are an artifact of the smoothing algorithm used to remove noise from the acceleration signals. The smoother produces a damping effect on the amplitude of the acceleration

oscillations, which, when compared to the ratios of force coefficients, produces the oscillations in the reconstructed states.

It should be noted that in general the reconstructed atmosphere states between the two reconstruction methods tend to agree much better in the supersonic region of flight (700-780 seconds) than in the hypersonic region (600-700 seconds) due to the presence of RCS thruster firings during large portions of the hypersonic regime. Additionally, an aerodynamic reconstruction [52] utilizing the heat shield pressure transducer measurements determined that axial force coefficient differed slightly from nominal during hypersonic flight, leading to noticeable deviations in the reconstructed states from the ADB reconstruction. The details of the aerodynamic reconstruction can be found in Refs. [52] and [53].

The Mach number and dynamic pressure results also compare favorably between the ADB and EKF reconstructions. Mach number observability tends to be very poor near entry interface due to the very low density in this part of the atmosphere. As such, differences at 600 seconds are on the order of Mach 1, but quickly reduce to less than 0.1 Mach at 650 seconds. Dynamic pressure differences are very reasonable, on the order of 5%-10% during the entire reconstruction region.

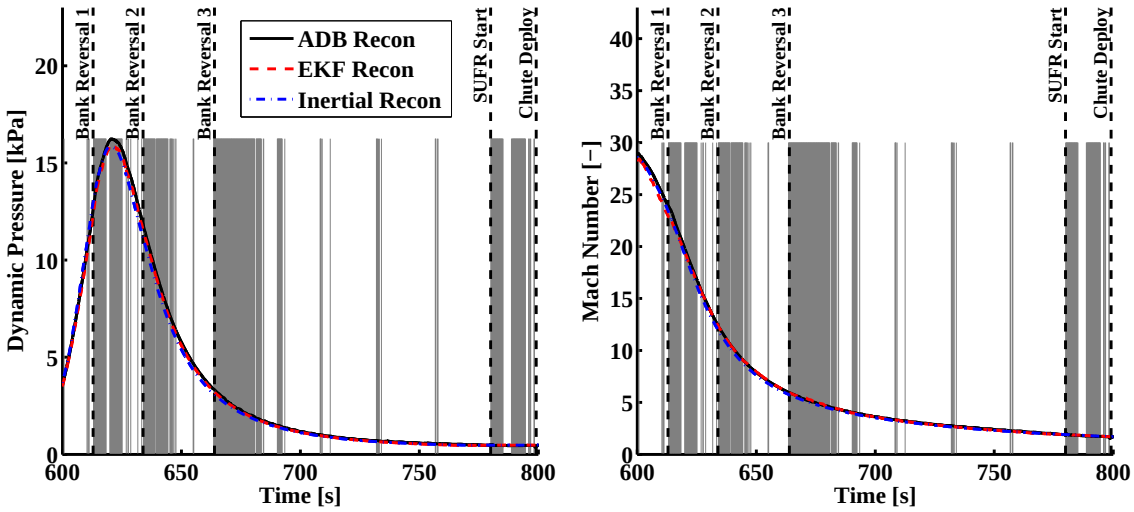

(a) Dynamic Pressure

(b) Mach Number

Figure 19: Air Data State Estimates

The estimates of wind-relative attitude (angle of attack and angle of sideslip) reconstructed by the three methods are presented in Fig. 20. While still in reasonably good agreement, larger discrepancies can be observed between the values generated by the two methods. As was the case for the atmosphere reconstruction, during

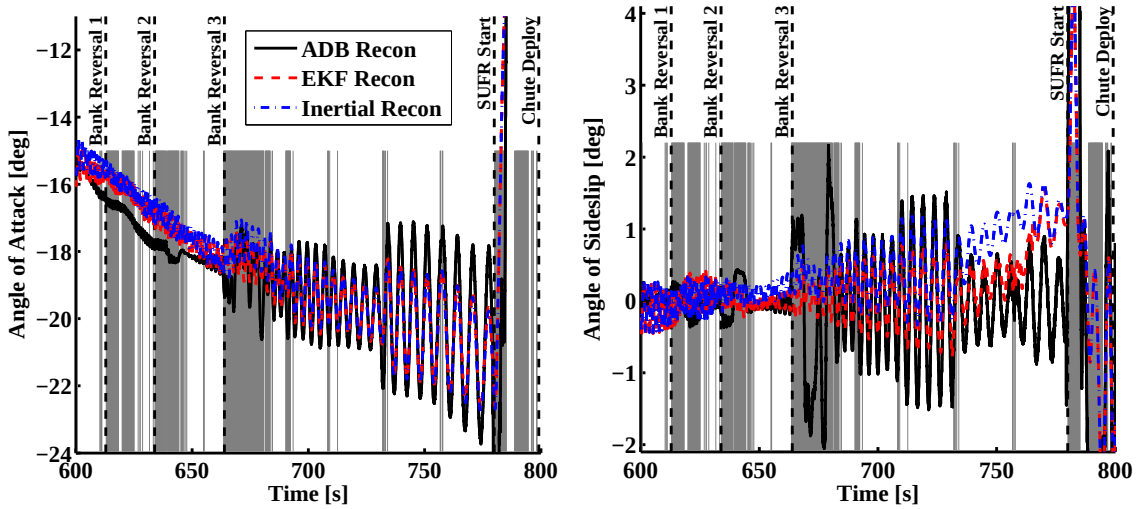

(a) Angle of Attack

(b) Angle of Sideslip

Figure 20: Wind-relative Attitude State Estimates

the hypersonic area of the trajectory a noticeable difference in angle of attack is observed. This discrepancy can be attributed to two factors: (1) the observation of non-aerodynamic forces by the IMU due to banking maneuvers performed by the vehicle and (2) an off-nominal axial force coefficient skewing the density results. As mentioned previously, the axial force coefficient was determined to be roughly 1% higher than the nominal value from the MSL aerodynamic database, yielding angle of attack values from the ADB reconstruction on the order of a degree lower than the EKF reconstruction. Note that during the supersonic regime of the trajectory, beyond 650 seconds, the ADB and EKF angle of attack profiles fall into much better agreement.

Angle of sideslip from the ADB method shows two very noticeable differences from the EKF reconstruction. The first is between 660 and 680 seconds, during the third and final bank maneuver during entry. The grey, shaded region covering that time span exactly overlaps a region of very large discrepancy between the two reconstructions. It can be concluded that the thruster firings during this region have caused the observed deviations in the ADB angle of sideslip. The second difference between the ADB and EKF angle of sideslip appears during the part of the trajectory before SUFR, roughly 760 to 780 seconds. This discrepancy is due to the presence of a persistent cross-wind on the order of 10-20 m/s. The EKF is able to observe wind environments during the trajectory through the pressure transducer measurements, but beyond 750 seconds, the measurements are below the intended range of

the transducers. At this point, the pressure measurements are transitioned out of the EKF because the uncertainty in their values is too large to provide meaningful observation of the atmosphere. After the pressure measurements are removed from the filter, the EKF is only relying on the mesoscale model which has no knowledge of the day of flight winds. As a result, the EKF angle of sideslip begins to deviate from the ADB sideslip during this period. Further detail on the wind environments observed through reconstruction during flight can be found in Ref. [54].

6.2 MSL State Uncertainties

The ADB state uncertainties are presented in Figs. 21-26. Each figure shows the difference between the ADB reconstruction and the EKF reconstruction with the 1-σ uncertainty bounds computed by the ADB uncertainty assessment. The atmosphere state uncertainties tend to be low in the hypersonic range with increasing values during the transition to supersonic flight. This can be attributed to the relatively low value of hypersonic C_A uncertainty (3%) versus supersonic C_A uncertainty (10%) for the MSL entry vehicle, as shown in Table 6.

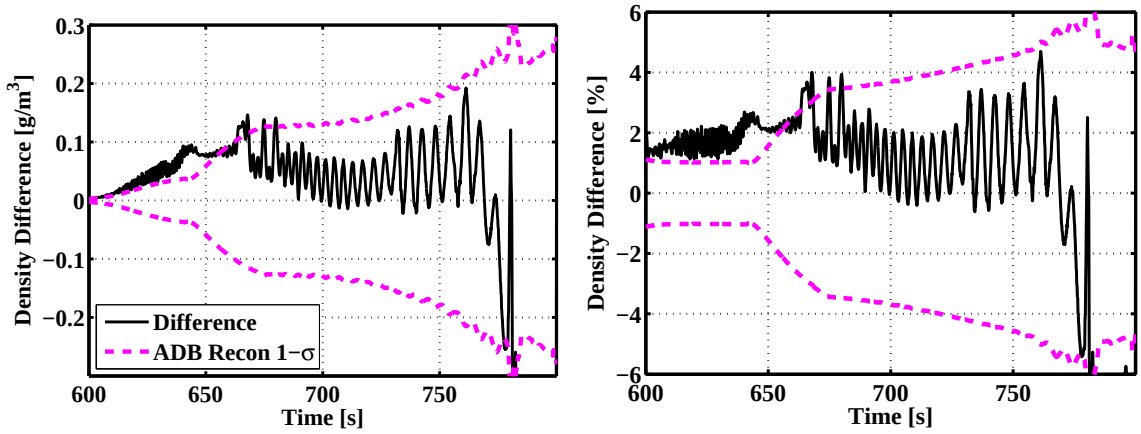

(a) Absolute Difference

(b) Percent Difference

Figure 21: Density Uncertainty

During the hypersonic regime, the atmosphere states exceed the 1-σ uncertainties because of the low uncertainty value as well as the known off-nominal hypersonic axial force behavior, mentioned in the previous section. Note that this behavior is also present in dynamic pressure and Mach number results. Density differences during this period are roughly 2% of the reconstructed value, while pressure and temperature differences are roughly 7% or less. Supersonic differences in atmosphere variables are also low, and well within the 1-σ uncertainties during that range.

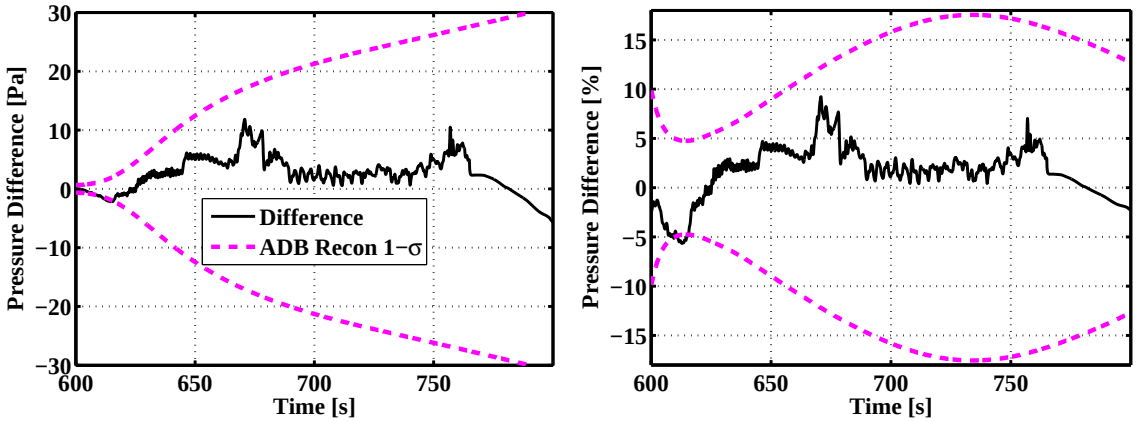

(a) Absolute Difference (b) Percent Difference

Figure 22: Pressure Uncertainty

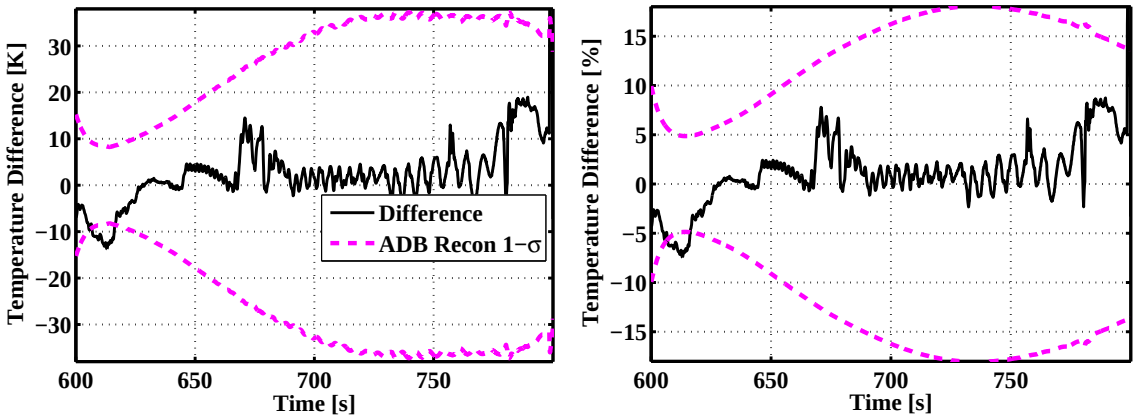

(a) Absolute Difference (b) Percent Difference

Figure 23: Temperature Uncertainty

Dynamic pressure differences through the trajectory are low, between 2% and 10%, but do not consistently fall inside of the 1-σ uncertainty bounds. As expected, the dynamic pressure uncertainties are driven by density (see Section 6.3), sharing a similar range of uncertainty between roughly 1% and 4%. Differences between the ADB and EKF dynamic pressure signals during the supersonic range begin to exceed the ADB uncertainty and continue to grow through the trajectory. As with the hypersonic results, it is suspected that this is due to off-nominal vehicle aerodynamics during this regime. The potential for deviations from the nominal value of C_A in the supersonic range are presented and discussed in Ref. [53]. It is also important to note that the EKF reconstruction is considered the best estimate of the state, but not the truth. Certainly, errors introduced during the EKF reconstruction could be causing

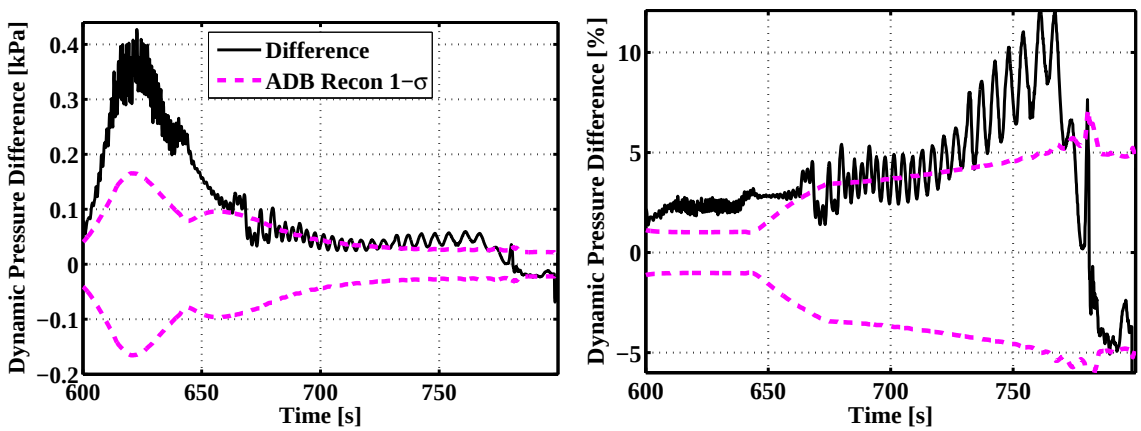

(a) Absolute Difference (b) Percent Difference

Figure 24: Dynamic Pressure Uncertainty

larger than expected discrepancies relative to the ADB uncertainty bounds. In spite of the 1-σ discrepancies seen for dynamic pressure, the reconstruction differences fall inside of the 3-σ bounds through the entire trajectory, which still lends confidence to the results from the ADB reconstruction.

Mach number uncertainties are large at the start of the trajectory due to the relatively low values of density in that region. Those uncertainties quickly reduce through the hypersonic phase and into the supersonic phase, reaching 1-σ levels below Mach 0.5 by 620 seconds and below Mach 0.25 by 730 seconds. As with atmosphere, the Mach number differences between the ADB and EKF reconstructions breach the 1-σ ADB uncertainties during the hypersonic regime and are well inside of the uncertainties during the supersonic regime.

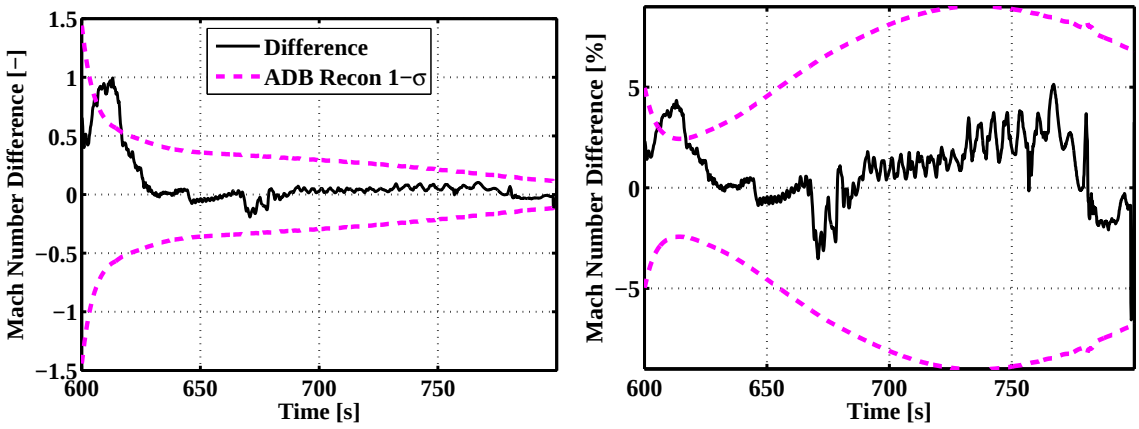

(a) Absolute Difference (b) Percent Difference

Figure 25: Mach Number Uncertainty

The uncertainties of angle of attack and sideslip also appear to be very reasonable with respect to the differences between the two reconstructions. The angle of attack difference reaches the 1-σ lower bound before 650 seconds, again due to the off-nominal value of C_A likely experienced by the vehicle. Angle of sideslip uncertainties bound the reconstruction differences very well aside from the region between 660 and 680 seconds, where RCS thruster firings disrupt the ADB reconstruction. The uncertainties on angle of attack and sideslip are just under one degree at the start of the trajectory and slowly increase over time. Angle of attack uncertainties reach values of roughly 2 degrees by the end of the trajectory, while angle of sideslip uncertainties grow to only 1.5 degrees.

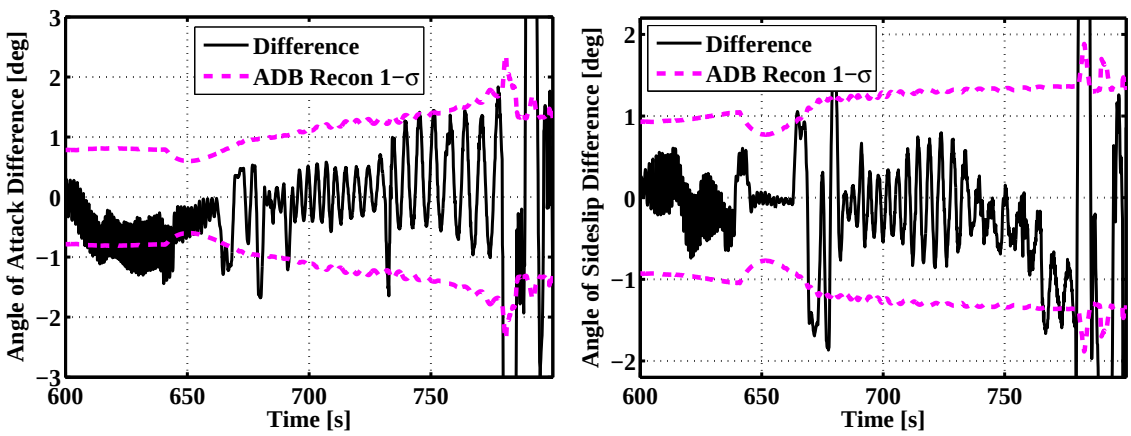

(a) Angle of Attack (b) Angle of Sideslip

Figure 26: Wind-relative Attitude State Uncertainties

Overall, the uncertainty assessment of each state from the ADB reconstruction provides very strong results in support of the accuracy of the state estimates. There does appear to be some conservatism in the uncertainties of atmosphere and Mach number in the supersonic portion of flight. This is clearly a result of the level of uncertainty carried by the MSL entry vehicle aerodynamics during this region. A 10% uncertainty in C_A is a fairly conservative estimate, which is reflected in the uncertainty of the reconstructed states. Overall, these results reinforce the importance of aerodynamic uncertainty with regards to the accuracy of this reconstruction approach. The ADB reconstruction uncertainties are further explored in the next section.

6.3 MSL Uncertainty Sensitivities

A sensitivity analysis of the ADB state uncertainties is conducted to examine the impact of each input uncertainty and understand the driving contributors. This analysis is performed through the linear covariance mapping technique, by decomposing the computed variance into components representing the contribution of each input variance to the output variance. As an example, consider the covariance mapping equation for dynamic pressure derived from Eq. 52:

$$\sigma_{\bar{q}}^2 = \boldsymbol{J}_{\bar{q}} \operatorname{cov}\left(\boldsymbol{w}_{\bar{q}}\right) \boldsymbol{J}_{\bar{q}}^T \tag{96}$$

Eq. 96 can be expanded as shown by Eq. 97. As mentioned in Section. 5.2, most inputs were assumed to be uncorrelated, as was the case for dynamic pressure.

$$\sigma_{\bar{q}}^2 = \begin{bmatrix} \frac{\partial \bar{q}}{\partial \rho} & \frac{\partial \bar{q}}{\partial V} \end{bmatrix} \begin{bmatrix} \sigma_\rho^2 & 0 \\ 0 & \sigma_V^2 \end{bmatrix} \begin{bmatrix} \frac{\partial \bar{q}}{\partial \rho} & \frac{\partial \bar{q}}{\partial V} \end{bmatrix}^T \tag{97}$$

The operations in Eq. 97 can be carried through, and the resulting expression is obtained, relating the input variances to the output variance:

$$\sigma_{\bar{q}}^2 = \left(\frac{\partial \bar{q}}{\partial \rho}\right)^2 \sigma_\rho^2 + \left(\frac{\partial \bar{q}}{\partial V}\right)^2 \sigma_V^2 \tag{98}$$

Now, the contributors to the dynamic pressure variance can be identified through the Jacobian matrix terms and the density and velocity variances. This assessment was performed for each state uncertainty to explore and identify driving inputs.

The atmosphere variance sensitivities are presented in Fig. 27 and Fig. 28. Pressure uncertainty is dominated by altitude and temperature uncertainty is dominated by pressure. The density uncertainty carries several contributors, including the uncertainty factors for axial force coefficient, divided into a hypersonic and supersonic multiplier as described by the uncertainty model shown in Section 5.2. Note that the prefixes ‘h’ and ‘s’ are used to denote the hypersonic and supersonic axial force multipliers. As expected, the contribution of uncertainty from the hypersonic multiplier diminishes and eventually disappears as the vehicle enters the supersonic regime. Conversely, the impact of the supersonic multiplier emerges and increases as the vehicle transitions from hypersonic to supersonic flight. Interestingly, the hypersonic axial force coefficient multiplier appears to drive density uncertainty during the hypersonic regime, while the axial acceleration uncertainty is the largest driver during the supersonic regime.

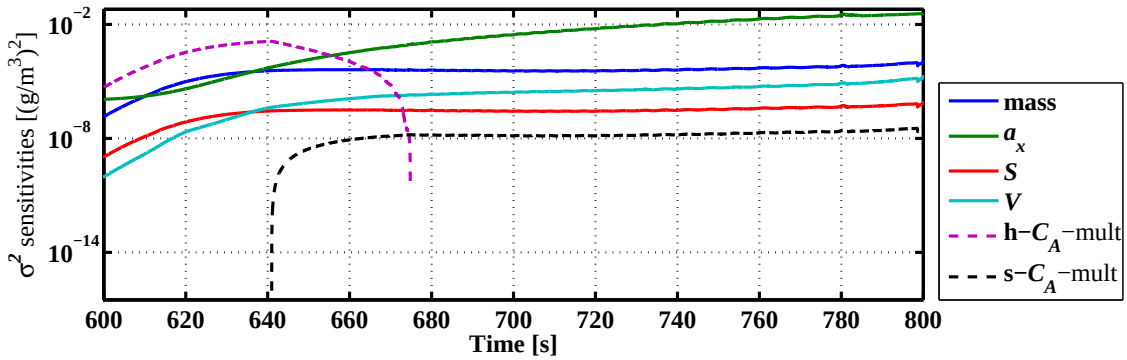

Figure 27: Density Variance Sensitivities

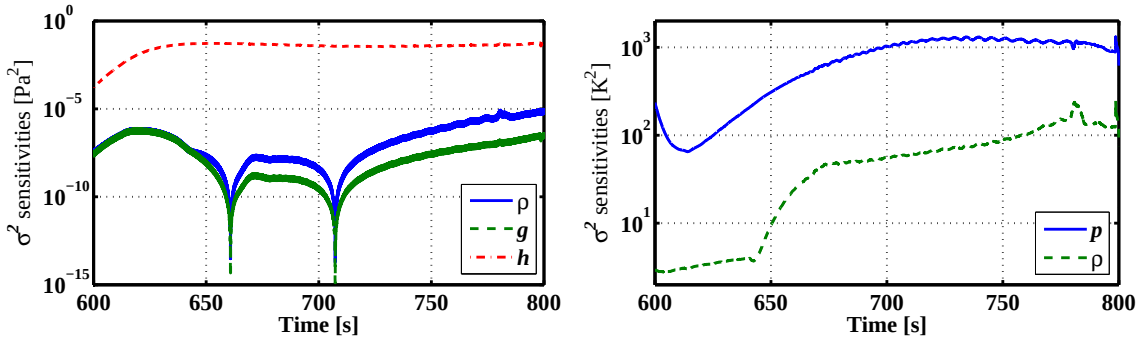

(a) Pressure

(b) Temperature

Figure 28: Pressure and Temperature Variance Sensitivities

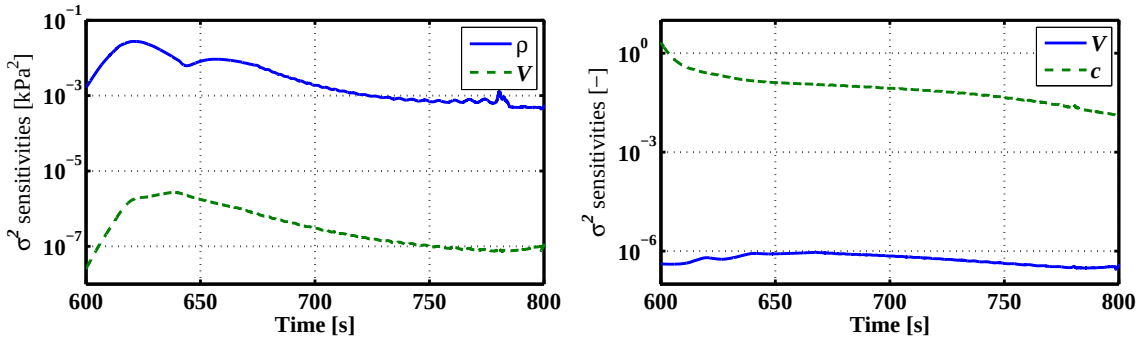

(a) Dynamic Pressure

(b) Mach Number

Figure 29: Air Data State Variance Sensitivities

The dynamic pressure and Mach number variance sensitivities are presented in Fig. 29. For dynamic pressure, velocity uncertainty, obtained from covariance mapping (Eq. 1), is driven by the IMU error specifications because the velocity is obtained through inertial reconstruction, while density uncertainty is driven by axial force coefficient and acceleration uncertainty as shown in Fig. 27. Thus, because of

the relatively large uncertainties in the vehicle aerodynamics, the driving input for dynamic pressure uncertainty is density. Mach number uncertainty is driven by speed of sound, which is also a function of density, again dominating the contribution of velocity.

The angle of attack and sideslip variance sensitivities are presented in Figs. 30 and 31. Due to the high number of aerodynamic contributors, each state is divided into subplots of the hypersonic and supersonic sensitivities. Each force coefficient uncertainty factor refers to the flight regime presented (i.e. C_A-mult in Fig. 30(a) refers to the hypersonic axial force multiplier), and the 'h/s' prefix used in the density sensitivity figure is dropped for the sake of space. The results reinforce the expectation that normal force coefficient uncertainty is the strongest contributor to angle of attack, and side force uncertainty is the strongest contributor to angle of sideslip. Conversely, side force uncertainty and normal force uncertainty tend to be the weakest uncertainty drivers for angle of attack and sideslip, respectively.

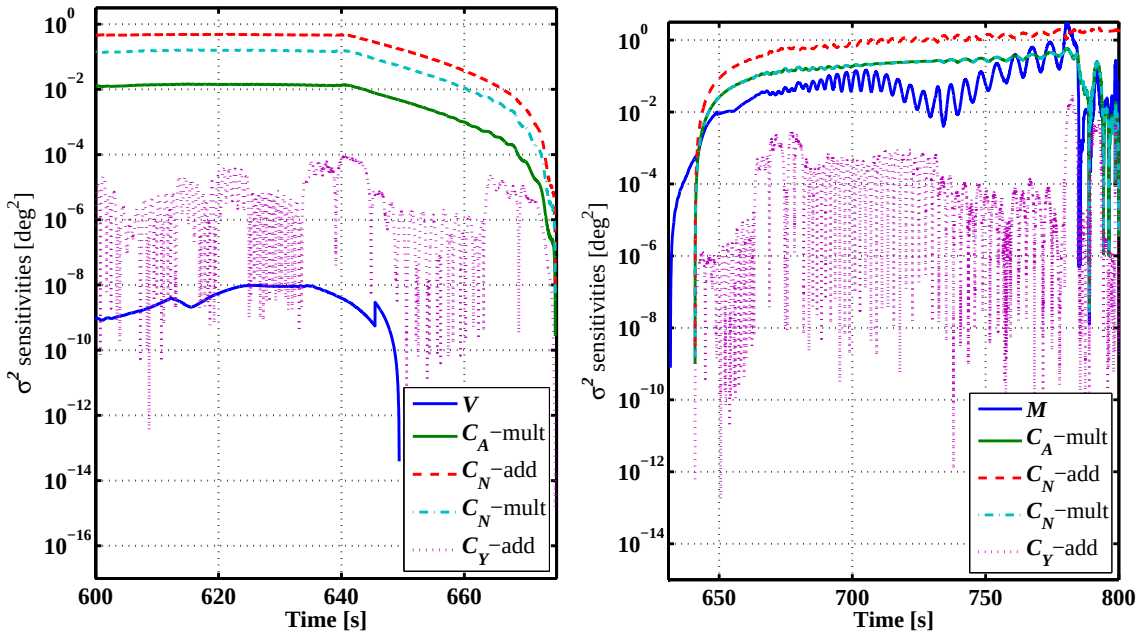

(a) Hypersonic Regime

(b) Supersonic Regime

Figure 30: Angle of Attack Variance Sensitivities

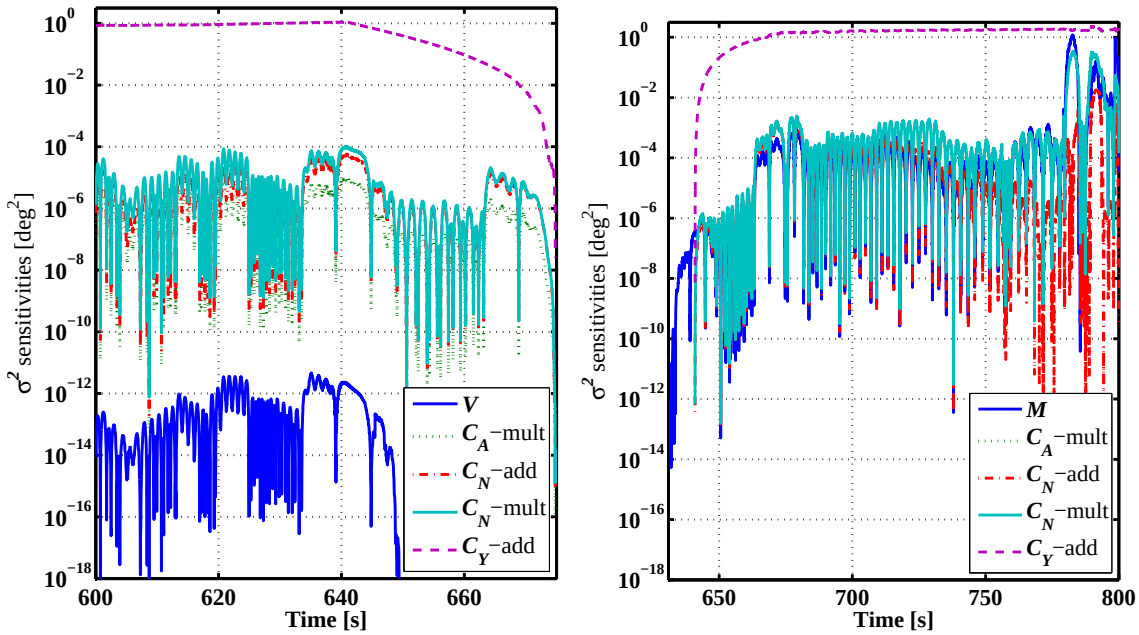

(a) Hypersonic Regime

(b) Supersonic Regime

Figure 31: Angle of Sideslip Variance Sensitivities

6.4 Discussion of Results

The results presented in the previous sections reveal some interesting findings regarding the ADB reconstruction method. The comparison of the reconstruction to alternate methods provides insight into where the ADB method is limited and where it can be used to complement the weaknesses of other reconstructions. The uncertainties, while conservative, provide a strong measure of confidence in the accuracy of the state estimates. Additionally, the uncertainty sensitivity study identifies inputs to the reconstruction that appear to drive the output uncertainties. These sensitivities provide valuable information regarding the input sources that, if improved, can increase the accuracy of the reconstruction.

Two important limitations of the ADB reconstruction method are confirmed by the MSL results: reconstruction errors due to (1) the presence of non-aerodynamic forces recorded by the IMU and (2) the existence of off-nominal vehicle aerodynamics during flight. The RCS firings during periods of dynamic maneuvering by the entry vehicle exposed regions where large deviations are apparent between the ADB results and the EKF and inertial reconstruction results. These deviations are most significant for the angle of attack and sideslip reconstructions because these states

are particularly sensitive to the vehicle dynamics. The presence of off-nominal aerodynamics, having been identified in other studies, affects the ADB reconstruction in the hypersonic regime where axial force coefficient is known to have differed from its pre-flight profile. In spite of these deviations, a majority of the reconstruction error (relative to the EKF) remains inside of uncertainties generated by the uncertainty assessment. Thus, while these limitations carry influence over the results, the reconstruction provides a useful source of post-flight data to complement and inform other reconstruction approaches.

The major advantage to the ADB reconstruction approach is its ability to compute in-flight estimates of the atmosphere and atmosphere-relative states. This allows for a more accurate characterization of trajectory parameters dependent on knowledge of the atmosphere. In fact, the ADB reconstruction can be used to identify issues with other reconstruction approaches where they may be limited. This is seen for the angle of sideslip profile, where a persistent cross wind results in a non-zero mean value of sideslip in the EKF and inertial reconstructions during the supersonic region of entry. This discrepancy was better understood by having the ADB reconstruction for comparison. Because the ADB method precludes the use of a reference atmosphere, it is unaffected by the presence of off-nominal atmospheric conditions.

The linear covariance mapping technique provides a very convenient method of identifying uncertainty contributors because input and output uncertainty are directly mapped. This type of assessment is not as easily obtained through other methods, such as the unscented transform which models the non-linearities of the process model in generating the output uncertainty, but does not have a way of extracting the input contributions. Although an unscented transform can provide higher order estimates of uncertainty, the ADB algorithm does not utilize strongly non-linear estimation equations, supporting the use of linear covariance transformations for accurate uncertainty quantification. In general, the uncertainty sensitivities address the fundamental concept underlying the ADB method - that the aerodynamics can be used to derive atmospheric properties. For the most part, uncertainty in aerodynamic knowledge of the vehicle drives the uncertainty of the reconstructed states. While improved aerodynamic accuracy is sought after in almost every realm of atmospheric flight, it is critical to the ADB reconstruction in deriving better estimates.

As a final note, the convergence details of the algorithm are recorded in order to understand the computational burden, in terms of number of iterations, of the ADB reconstruction. The number of iterations performed by the algorithm for both the inner loop and outer loop at each time are shown in Fig. 32. Note that the inner

loop iteration number refers to the maximum number of iterations over the number of outer loop iterations at each time. The algorithm converges a majority of the time in two to four iterations (both inner and outer loop), and increases towards the end of the trajectory. The maximum number of iterations for convergence is nine for the outer loop and eight for the inner loop. These maximum values appear near the SUFR maneuver where the trajectory becomes very dynamic and changes in vehicle attitude occur at a higher rate.

Overall, the results show only a small computational effort required by the algorithm in order to achieve final state estimates. The iteration number results support the potential for the use of the ADB estimation approach inside of a flight software algorithm for guidance and navigation of an entry vehicle. This would be a very interesting application of the research presented in this thesis.

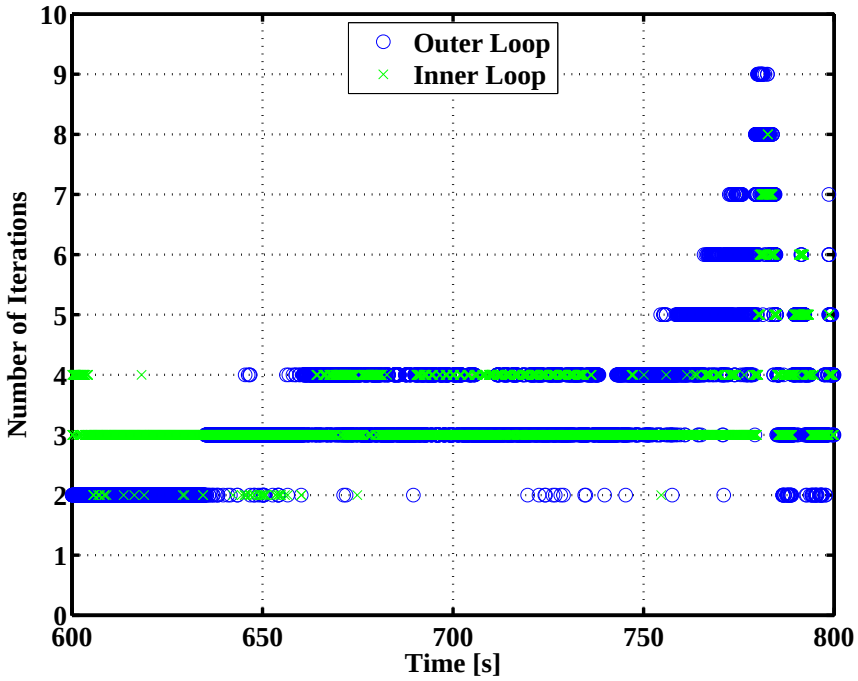

Figure 32: Number of Iterations Inside of ADB Algorithm

CHAPTER VII

CONCLUSIONS AND FORWARD RESEARCH

The objective of this thesis is to develop a method of trajectory reconstruction well suited for entry, descent and landing missions to planets other than Earth. The underlying problem being addressed is the relatively large uncertainty in atmosphere for these types of missions, resulting in inaccurate reconstruction of atmosphere-relative states. To that end, a methodology is presented for atmosphere and atmosphere-relative parameter reconstruction by which state estimates are computed through the known aerodynamics of the vehicle. Additionally, uncertainties of each reconstructed output are derived through linear covariance mapping, transforming input variances to output uncertainties. The ADB reconstruction algorithm developed in this thesis is applied to the MSL EDL flight data and compared against two alternate reconstruction approaches, an inertial reconstruction and an EKF reconstruction. The results were used to evaluate the performance of the algorithm and assess the generated uncertainties.

Overall, the results provide a strong degree of confidence in the ADB reconstruction method. The simplicity of the approach is its greatest advantage, in that an EDL vehicle carrying only an IMU can use the technique to reconstruct crucial trajectory states. In spite of this advantage, the ADB algorithm is not intended to stand alone as a singular approach to trajectory reconstruction. Rather, it should be coupled with other reconstruction techniques in reconciling discrepancies to support a best estimate of the vehicle entry conditions as was done on many past planetary exploration missions. In this way, a more complete picture of the flight profile can be obtained to provide the greatest possible benefit to future missions and, more generally, planetary exploration.

Although the methodology developed for this thesis can be readily applied for current and future problems, there are avenues of interest that can be explored as future research topics. The first is the application of the ADB algorithm for real-time problems. As mentioned in the previous section, the computational requirements of the algorithm make it relatively appealing for use onboard an entry vehicle for the purposes of guidance and navigation. In-flight knowledge of atmosphere and wind-relative attitude could allow for reduction in size of the landing ellipse or the targeting

of more challenging landing sites not previously explored. The second item of future work is in identifying correlations to include in the input covariance matrices used by the ADB uncertainty mapping. For the most part, these terms are assumed to be zero. Accounting for input correlations would have the benefit of removing some of the conservatism observed by the estimated state uncertainties. For the purposes of the analysis conducted in this research, the overly conservative estimates were deemed a more satisfactory result than the potential for overly generous uncertainty estimates. The final item of future exploration is the application of an alternate uncertainty assessment technique, such as an unscented transform. This could result in an improved estimate of uncertainty where non-linearities in the estimation equations may limit the linear covariance transformation used in this research. With these ideas in mind going forward, it is anticipated that this research will be of value to engineers performing reconstruction of entry trajectories to evaluate vehicle performance in the hopes of expanding the objectives of future EDL missions.

APPENDIX A

EULER INTEGRATION OF HYDROSTATIC EQUATION

The hydrostatic equation expresses a relationship between an infinitesimally small change in pressure to an infinitesimally small change in altitude for a differential volume of a fluid element. Hydrostatic equilibrium satisfies the following differential equation:

$$dp = -\rho g dh \tag{99}$$

In the equation above, dp and dh are the pressure and height of an infinitesimally small fluid element with density, ρ, and local acceleration due to gravity, g. For the research presented in this thesis, an Euler integrator is used to obtain a closed form expression for pressure:

$$X_k = X_{k-1} + \dot{X}_{k-1} dt \tag{100}$$

where X_k is the state at the current integration step, X_{k-1} is the state at the previous integration step, $\dot{X}_{k-1}$ is the derivative of the state evaluated at the previous integration step and dt is the integration step size. This expression for the Euler integration scheme can be applied to obtain a relationship for pressure by substituting pressure, p, for the generalized state, X, and the hydrostatic equation for the derivative of the state in Eq. 100:

$$p_k = p_{k-1} + \frac{dp}{dh} dh \tag{101}$$

$$p_k = p_{k-1} + (-\rho_k g_k)\, dh \tag{102}$$

$$p_k = p_{k-1} - \rho_k g_k (h_k - h_{k-1}) \tag{103}$$

Eq. 103 is the expression used to integrate the hydrostatic equation by propagating pressure from the maximum to the minimum altitude of the trajectory.

APPENDIX B

PARTIAL DERIVATIVE EXPRESSIONS FOR AIR DATA UNCERTAINTY ASSESSMENT

Recall that a linear covariance mapping technique is used to map the input uncertainties to output variances for all of the states estimated by the ADB reconstruction algorithm. For this approach, the partial derivatives of each estimation equation are taken with respect to the inputs in order to assemble the Jacobian matrix used to transform the uncertainties. In Section 4.2, the partial derivative expressions needed for the uncertainty assessment of pressure, angle of attack and angle of sideslip are given. The partial derivative expressions for the remaining air data states are not provided in the section in order to keep a reasonable number of analytic partial derivative equations in the main part of the thesis. This appendix will detail the partial derivatives of pressure, Mach number, temperature and dynamic pressure with respect to the inputs of each equation.

The pressure equation, given in Section 3.1.1 is:

$$p_k = p_{k-1} - \rho_k g_k \left(h_k - h_{k-1}\right) \tag{104}$$

The partial derivatives of the pressure equation are evaluated analytically:

$$\frac{\partial p_k}{\partial p_{k-1}} = 1 \tag{105}$$

$$\frac{\partial p_k}{\partial \rho_k} = -g_k \left(h_k - h_{k-1}\right) \tag{106}$$

$$\frac{\partial p_k}{\partial g_k} = -\rho_k \left(h_k - h_{k-1}\right) \tag{107}$$

$$\frac{\partial p_k}{\partial h_k} = -\rho_k g_k \tag{108}$$

$$\frac{\partial p_k}{\partial h_{k-1}} = \rho_k g_k \tag{109}$$

In order to obtain Mach uncertainty, speed of sound uncertainty must also be mapped. Although speed of sound is not an output state of the ADB reconstruction, it is computed internally by the algorithm. The equation for speed of sound, given in Secion 3.1.1 is:

$$c_k = \sqrt{\gamma \frac{p_k}{\rho_k}} \tag{110}$$

The partial derivatives of the speed of sound equation are evaluated analytically:

$$\frac{\partial c_k}{\partial p_k} = \frac{1}{2}\sqrt{\frac{\gamma}{p_k \rho_k}} \tag{111}$$

$$\frac{\partial c_k}{\partial \rho_k} = -\frac{1}{2\rho_k}\sqrt{\frac{\gamma p_k}{\rho_k}} \tag{112}$$

Using the speed of sound uncertainty computed through the partial derivatives above, the Mach number uncertainty can be computed next. The equation for Mach number is:

$$M_k = \frac{V_k}{c_k} \tag{113}$$

The partial derivatives of the Mach number equation are evaluated analytically:

$$\frac{\partial M_k}{\partial V_k} = \frac{1}{c_k} \tag{114}$$

$$\frac{\partial M_k}{\partial c_k} = -\frac{V_k}{c_k^2} \tag{115}$$

Next, the temperature equation is:

$$T = \frac{p_k}{\rho_k R} \tag{116}$$

The partial derivatives of the temperature equation are evaluated analytically:

$$\frac{\partial T_k}{\partial p_k} = \frac{1}{\rho_k R} \tag{117}$$

$$\frac{\partial T_k}{\partial \rho_k} = -\frac{p_k}{\rho_k^2 R} \tag{118}$$

Finally, the dynamic pressure equation is:

$$\bar{q}_k = \frac{1}{2}\rho_k V_k^2 \tag{119}$$

The partial derivatives of the dynamic pressure equation are evaluated analytically:

$$\frac{\partial \bar{q}_k}{\partial \rho_k} = \frac{1}{2}V_k^2 \tag{120}$$

$$\frac{\partial \bar{q}_k}{\partial V} = \rho_k V_k \tag{121}$$

REFERENCES

[1] Furniss, T., *A History of Space Exploration*, Mercury Books, London, 2005.

[2] Braun, R. D. and Manning, R., "Mars Exploration Entry, Descent, and Landing Challenges," *Journal of Spacecraft and Rockets*, Vol. 44, No. 2, March-April 2007, pp. 310–323.

[3] Ingoldby, R., Michel, F., Flaherty, T., Doty, M., Preston, B., Villyard, K., and Steele, R., "Entry Data Analysis for Viking Landers 1 and 2," NASA CR-159388, November 1976.

[4] Pruett, C., Wolf, H., Heck, M., and Siemers, P., "Innovative Air Data System for the Space Shuttle Orbiter," *Journal of Spacecraft and Rockets*, Vol. 20, No. 1, 1983, pp. 61–69.

[5] Takaki, R. and Tazikawa, M., "ADS Measurements of HYFLEX (HYpersonic FLight EXperiment)," AIAA Paper 97-0193, January 1997.

[6] Whitmore, S., Cobleigh, B., and Haering, E., "Design and Calibration of the X-33 Flush Airdata Sensing (FADS) System," AIAA Paper 98-0201, January 1998.

[7] Cobleigh, B., Whitmore, S., Haering, E., Borrer, J., and Roback, V., "Flush Airdata Sensing (FADS) System Calibration Procedures and Results for Blunt Forebodies," AIAA Paper 99-4816, November 1999.

[8] Farrell, J. A. and Barth, M., *The Global Positioning System & Inertial Navigation*, McGraw-Hill, New York, NY, 1999.

[9] Titterton, D. and Weston, J., *Strapdown Inertial Navigation Technology*, The Institution of Electrical Engineers, Stevenage, United Kingom, 2004.

[10] Karlgaard, C., Kutty, P., Schoenenberger, M., Shidner, J., and Munk, M., "Mars Entry Atmospheric Data System Trajectory Reconstruction Algorithms and Flight Results," AIAA Paper 2013-0028, January 2013.

[11] Simon, D., *Optimal State Estimation*, John Wiley & Sons, Inc., Hoboken, NJ, 2006.

[12] Schmidt, S. F., "The Kalman Filter: Its Recognition and Development for Aerospace Applications," *Journal of Guidance and Control*, Vol. 4, No. 1, 1981, pp. 4–7.

[13] Karlgaard, C., Kutty, P., Schoenenberger, M., and Shidner, J., "Mars Science Laboratory Entry, Descent, and Landing Trajectory and Atmosphere Reconstruction," AAS Paper 13-307, 2013.

[14] Nørgaard, M., Poulsen, N., and Ravn, O., "New developments in state estimation for nonlinear systems," *Automatica*, Vol. 36(11), November 2000, pp. 1627–1638.

[15] Karlgaard, C. and Shen, H., "Desensitized Kalman filtering," *IET Radar, Sonar and Navigation*, Vol. 7(1), 2013, pp. 2–9.

[16] Seiff, A., "Some Possibilities for Determining the Characteristics of the Atmospheres of Mars and Venus from Gas-Dynamic Behavior of a Probe Vehicle," NASA TN D-1770, 1963.

[17] Sommer, S. and Yee, L., "An Experiment to Determine the Structure of a Planetary Atmosphere," AIAA Paper 68-1054, October 1968.

[18] Seiff, A., Reese, D., Sommer, C., Kirk, D., Whiting, E., and Niemann, H., "PAET, An Entry Probe Experiment in the Earth's Atmosphere," *Icarus*, Vol. 18, 1973, pp. 525–563.

[19] Seiff, A., Kirk, D., Young, R., Blanchard, R., Findlay, J., Kelly, G., and Sommer, S., "Measurements of Thermal Structure and Thermal Contrasts in the Atmosphere of Venus and Related Dynamical Observations: Results From the Four Pioneer Venus Probes," *Journal of Geophysical Research*, Vol. 85, No. A13, December 1980, pp. 7903–7933.

[20] Seiff, A., Kirk, D., Knight, T., Young, L., Milos, F., Venkatapathy, E., Mihalov, J., Blanchard, R., Young, R., and Schubert, G., "Thermal Structure of Jupiter's Upper Atmosphere Derived from the Galileo Probe," *Science*, Vol. 276, No. 5309, 1997, pp. 102–104.

[21] Kerzhanovich, V., "Mars 6: Improved Analysis of the Descent Module Measurements," *Icarus*, Vol. 30, 1977, pp. 1–25.

[22] Avduevsky, V., Marov, M., Rozhdestvensky, M., Borodin, N., and Kerzhanovich, M., "Soft Landing of Venera 7 on the Venus Surface and Preliminary Results of Investigations of the Venus Atmosphere," *Journal of Atmospheric Sciences*, Vol. 28, March 1971, pp. 263–269.

[23] Kazeminejad, B., Atkinson, D., Perez-Ayucar, M., Lebreton, J.-P., and Sollazzo, C., "Huygens' entry and descent through Titan's atmosphere - Methodology and results of the trajectory reconstruction," *Planetary and Space Science*, Vol. 55, 2007, pp. 1845–1876.

[24] Spencer, D. A., Blanchard, R. C., Braun, R. D., Kallemeyn, P. H., and Thurman, S. W., "Mars Pathfinder Entry, Descent, and Landing Reconstruction," *Journal of Spacecraft and Rockets*, Vol. 36, No. 3, May-June 1999, pp. 357–366.

[25] Withers, P. and Smith, M., "Atmospheric entry profiles from the Mars Exploration Rovers Spirit and Opportunity," *Icarus*, Vol. 185, 2006, pp. 133–142.

[26] Blanchard, R. and Desai, P., "Mars Phoenix Entry, Descent, and Landing Trajectory and Atmosphere Reconstruction," *Journal of Spacecraft and Rockets*, Vol. 48, No. 5, September-October 2011, pp. 809–821.

[27] Seiff, A. and Reese, D., "Use of Entry Vehicle Responses to Define the Properties of the Mars Atmosphere," *Advances in the Astronautical Sciences*, Vol. 19, 1965, pp. 419–444.

[28] Nier, A., Hanson, W., McElroy, M., Seiff, A., and Spencer, N., "Entry Science Experiment for Viking 1975," *Icarus*, Vol. 16, 1972, pp. 74–91.

[29] Spencer, D. A., Blanchard, R., Braun, R. D., Peng, C., and Kallemeyn, P. H., "Mars Pathfinder Atmospheric Entry Reconstruction," AAS Paper 98-146, 1998.

[30] Peterson, V., "A Technique for Determining Planetary Atmosphere Structure from Measured Accelerations of an Entry Vehicle," NASA TN D-2669, February 1965.

[31] Seiff, A., "Direct Measurements of Planetary Atmospheres by Entry Probes," Preprint AAS 68-187, Conference on Advanced Space Experiments, October 1968.

[32] Seiff, A., "Measurements in the Atmosphere of Mars," *Applied Optics*, Vol. 8, No. 7, July 1969, pp. 1305–1314.

[33] Magalhaes, J., Schofield, J., and Seiff, A., "Results of the Mars Pathfinder atmospheric structure investigation," *Journal of Geophysical Research*, Vol. 104, No. E4, April 1999, pp. 8943–8955.

[34] Withers, P., Towner, M., Hathi, B., and Zarnecki, J., "Analysis of entry accelerometer data: A case study of Mars Pathfinder," *Planetary and Space Science*, Vol. 51, 2003, pp. 541–561.

[35] Atkinson, D., Kazeminejad, B., Gaborit, V., Ferri, F., and Lebreton, J.-P., "Huygens probe entry and descent trajectory analysis and reconstruction techniques," *Planetary and Space Science*, Vol. 53, 2005, pp. 586–593.

[36] Colombatti, G., Withers, P., Ferri, F., Aboudan, A., Ball, A., Bettanini, C., Gaborit, V., Harri, A., Hathi, B., Leese, M., Makinen, T., Stoppato, P., Towner, M., Zarnecki, J., Angrilli, F., , and Fulchignoni, M., "Reconstruction of the trajectory of the Huygens probe using the Huygens Atmospheric Structure Instrument (HASI)," *Planetary and Space Science*, Vol. 56, 2008, pp. 586–600.

[37] Withers, P., "Trajectory and atmospheric structure from entry probes: Demonstration of a real-time reconstruction technique using a simple direct-to-Earth radio link," *Planetary and Space Science*, Vol. 58, 2010, pp. 2044–2049.

[38] Vallado, D. A., *Fundamentals of Astrodynamics and Applications*, Microcosm Press and Springer, New York, NY, 2007.

[39] Ellis, R. and Gulick, D., *Calculus*, Thomas Learning Custom Publishing, Mason, OH, 2003.

[40] North American Aviation, Inc., "Aerodynamic Data Manual for Project Apollo," Report SID 64-174C, 1965.

[41] King, A., "Inertial Navigation - Forty Years of Evolution," *GEC Review*, Vol. 3, No. 3, 1998, pp. 140–149.

[42] Regan, F. J. and Anandakrishnan, S. M., *Dynamics of Atmospheric Re-Entry*, American Institute of Aeronautics and Astronautics, Inc., Washington, D.C., 1993.

[43] Ku, H., "Notes on the Use of Propagation of Error Formulas," *Journal of Research of the National Bureau of Standards*, Vol. 70C, No. 4, October-December 1996, pp. 263–273.

[44] Montgomery, D. C. and Runger, G. C., *Applied Statistics and Probability for Engineers*, John Wiley & Sons, Inc., 2011.

[45] Schoenenberger, M., Dyakonov, A., Buning, P., Scallion, W., and Van Norman, J., "Aerodynamic Challenges for the Mars Science Laboratory Entry, Descent and Landing," AIAA Paper 2009-3914, June 2009.

[46] Steltzner, A. D., Burkhart, P. D., Chen, A., Comeaux, K. A., Guernsey, C. S., Kipp, D. M., Lorenzoni, L. V., Mendeck, G. F., Powell, R. W., Rivellini, T. P., San Martin, A. M., Sell, S. W., Prakash, R., , and Way, D. D., "Mars Science Laboratory Entry, Descent, and Landing System Overview," 7th International Planetary Probe Workshop, Barcelona, Spain, June 2010.

[47] Coatta, D., "MSL Mass Properties Report," IOM 352M-DMC-1017, October 2011.

[48] Van Norman, J., "Comparison of MSL Heatshield Metrology to CFD Grids and Analytical Surface Definition," Internal Memorandum, March 2011.

[49] Sirlin, S. W. and Vanelli, C., "MSL EDL KAST MIMU Model Implementation," Jet Propulsion Laboratory, EM 343H, January 2008.

[50] Scholz, D., "Dimensional Inspection of the MSLA Heat Shield 2 (PICA Heat Shield)," MSL-ST-11-0056, July 2011.

[51] Chen, A., Cianciolo, A., Vasavada, A., Karlgaard, C., Barnes, J., Cantor, B., Kass, D., Rafkin, S., and Tyler, D., "Reconstruction of Atmospheric Properties from the Mars Science Laboratory Entry, Descent, and Landing," *Journal of Spacecraft and Rockets*, Under Review.

[52] Schoenenberger, M., Van Norman, J., Karlgaard, C., Kutty, P., and Way, D. D., "Assessment of the Reconstructed Aerodynamics of the Mars Science Laboratory Entry Vehicle," *Journal of Spacecraft and Rockets*, Under Review.

[53] Schoenenberger, M., Van Norman, J., Dyakonov, A., Karlgaard, C., Way, C., and Kutty, P., "Assessment of the Reconstructed Aerodynamic of the Mars Science Laboratory Entry Vehicle," AAS paper 13-306, 2013.

[54] Karlgaard, C., Kutty, P., Schoenenberger, M., Munk, M., Little, A., Kuhl, C., and Shidner, J., "Mars Entry Atmospheric Data System Trajectory and Atmosphere Reconstruction of the Mars Science Laboratory Entry, Descent, and Landing," *Journal of Spacecraft and Rockets*, Under Review.